

CERN-EP-2017-050
2017/08/29

CMS-TOP-15-008

Measurement of the top quark mass in the dileptonic $t\bar{t}$ decay channel using the mass observables $M_{b\ell}$, M_{T2} , and $M_{b\ell\nu}$ in pp collisions at $\sqrt{s} = 8$ TeV

The CMS Collaboration*

Abstract

A measurement of the top quark mass (M_t) in the dileptonic $t\bar{t}$ decay channel is performed using data from proton-proton collisions at a center-of-mass energy of 8 TeV. The data was recorded by the CMS experiment at the LHC and corresponds to an integrated luminosity of $19.7 \pm 0.5 \text{ fb}^{-1}$. Events are selected with two oppositely charged leptons ($\ell = e, \mu$) and two jets identified as originating from b quarks. The analysis is based on three kinematic observables whose distributions are sensitive to the value of M_t . An invariant mass observable, $M_{b\ell}$, and a ‘stransverse mass’ observable, M_{T2} , are employed in a simultaneous fit to determine the value of M_t and an overall jet energy scale factor (JSF). A complementary approach is used to construct an invariant mass observable, $M_{b\ell\nu}$, that is combined with M_{T2} to measure M_t . The shapes of the observables, along with their evolutions in M_t and JSF, are modeled by a nonparametric Gaussian process regression technique. The sensitivity of the observables to the value of M_t is investigated using a Fisher information density method. The top quark mass is measured to be 172.22 ± 0.18 (stat) $^{+0.89}_{-0.93}$ (syst) GeV.

Published in Physical Review D as doi:10.1103/PhysRevD.96.032002.

1 Introduction

The top quark mass is a fundamental parameter of the standard model (SM), and an important component in global electroweak fits evaluating the self-consistency of the SM [1]. In addition, the value of M_t has implications for the stability of the SM electroweak vacuum due to the role of the top quark in the quartic term of the Higgs potential [2]. Measurements of M_t have been conducted by the CDF and D0 experiments at the Tevatron, and by the ATLAS and CMS experiments at the CERN LHC. These measurements are typically calibrated against the top quark mass parameter in Monte Carlo (MC) simulation. Studies suggest that this parameter can be related to the top quark mass in a theoretically well-defined scheme with a precision of about 1 GeV [3]. A combination of measurements including all four experiments and $t\bar{t}$ decay channels with zero, one, or two high- p_T electrons or muons (all-hadronic, semileptonic, and dileptonic, respectively) gives a value of 173.34 ± 0.36 (stat) ± 0.67 (syst) GeV [4] for the top quark mass. Currently, the most precise experimental determination of M_t is provided by CMS using a combination of measurements in all $t\bar{t}$ decay channels, yielding a value of 172.44 ± 0.13 (stat) ± 0.47 (syst) GeV [5]. In the dileptonic $t\bar{t}$ decay channel, the ATLAS [6] and CMS [5] Collaborations have recently determined M_t to be 172.99 ± 0.41 (stat) ± 0.74 (syst) GeV and 172.82 ± 0.19 (stat) ± 1.22 (syst) GeV, respectively. This paper presents a reanalysis of the dileptonic $t\bar{t}$ data set recorded in 2012, with a primary motivation of reducing the systematic uncertainties in M_t determination.

The dileptonic top quark pair ($t\bar{t}$) decay topology, $t\bar{t} \rightarrow (b\ell^+\nu)(\bar{b}\ell^-\bar{\nu})$, with $\ell = (e, \mu)$, presents a challenge in mass measurement arising primarily from the presence of two neutrinos in the final state. While the undetected \vec{p}_T of a single final-state neutrino in a semileptonic $t\bar{t}$ decay can be inferred from the momentum imbalance in the event, the allocation of momentum imbalance between the two neutrinos in a dileptonic $t\bar{t}$ decay is unknown a priori. For this reason, the dileptonic $t\bar{t}$ system is kinematically underconstrained, and mass determination cannot be easily conducted on an event-by-event basis. Instead, the mass of the parent top quarks in the dileptonic $t\bar{t}$ system can be extracted from kinematic features over an ensemble of events, with the help of appropriate observables and reconstruction techniques.

The measurement reported in this paper is based on a set of observables that have been proposed specifically for mass reconstruction in underconstrained decay topologies. These observables include the invariant mass, $M_{b\ell}$, of a $b\ell$ system, a ‘stransverse mass’ variable, M_{T2}^{bb} , constructed with the b and \bar{b} daughters of the $t\bar{t}$ system [7–9], and the invariant mass of a $b\ell\nu$ system, $M_{b\ell\nu}$, where the neutrino momentum is estimated by the M_{T2} -assisted on-shell (MAOS) reconstruction technique [10]. The MAOS reconstruction technique builds on M_{T2} by exploiting the neutrino momenta estimates that are by-products of the M_{T2} algorithm. The sensitivity of the $M_{b\ell}$, M_{T2}^{bb} , and $M_{b\ell\nu}$ observables to the value of M_t is investigated using a Fisher information density method. Distributions of $M_{b\ell}$ and M_{T2}^{bb} in dileptonic events contain a sharp edge descending to a kinematic endpoint, the location of which is sensitive to the value of M_t . Recently, masses of the top quark, W boson (M_W), and neutrino (M_ν) were extracted in a simultaneous fit using the endpoints of these distributions in dileptonic $t\bar{t}$ events [11]. The $M_{b\ell}$, M_{T2}^{bb} , and MAOS $M_{b\ell\nu}$ observables are described in more detail in Section 4.

One of the dominant sources of systematic uncertainty limiting the precision of this measurement comes from the overall uncertainty in jet energy scale (JES). To address the JES uncertainty, we introduce a technique that uses the $M_{b\ell}$ and M_{T2}^{bb} observables to determine an overall jet energy scale factor (JSF) simultaneously with the top quark mass, where the JSF is defined as a multiplicative factor scaling the four-vectors of all jets in the event. Similar techniques have been developed for the all-hadronic and semileptonic $t\bar{t}$ channels, where the jet pair originat-

ing from a W boson decay is used to determine the JSF [5]. Because light-quark jets from the W boson decay are used to calibrate the energy scale of b jets arising from the t and \bar{t} decays, these methods are sensitive to flavor-dependent uncertainties that emerge from differences in the response of b jets and light-quark jets. In the method featured here, the JSF is determined in the dileptonic $t\bar{t}$ channel without relying on a W boson decaying to jets. Instead, it achieves sensitivity to the JSF through the kinematic differences between b jets, which are subject to JSF scaling, and leptons, which are not. Because it does not use light quarks from a hadronic W boson decay, this approach is insensitive to flavor-dependent JES uncertainties.

To model the $M_{b\ell}$, M_{T2}^{bb} , and MAOS $M_{b\ell\nu}$ distribution shapes, we use a Gaussian process (GP) regression technique [12, 13]. This technique is nonparametric, and thus largely model-independent. It is effective in modeling distribution shapes when no theoretical guidance is available to specify a functional form. The distribution shapes can conveniently be modeled as functions of multiple variables. In this analysis, three variables are used: the value of the relevant observable ($M_{b\ell}$, M_{T2}^{bb} , or $M_{b\ell\nu}$), M_t , and the JSF. The shapes are determined using simulated events generated with seven different values of M_t ranging from 166.5 to 178.5 GeV, and with five values of JSF, ranging from 0.97 to 1.03, applied to the jets in each event. Each shape ultimately models the distributions of the observables together with their evolution in M_t and in JSF.

2 The CMS detector

The central feature of the CMS apparatus is a superconducting solenoid of 6 m internal diameter, providing a magnetic field of 3.8 T. Within the solenoid volume are a silicon pixel and strip tracker, a lead tungstate crystal electromagnetic calorimeter (ECAL), and a brass and scintillator hadron calorimeter (HCAL), each composed of a barrel and two endcap sections. The tracker has a track-finding efficiency of more than 99% for muons with transverse momentum $p_T > 1$ GeV and pseudorapidity $|\eta| < 2.4$. The ECAL is a fine-grained hermetic calorimeter with quasi-projective geometry, and is distributed in the barrel region of $|\eta| < 1.48$ and in two endcaps that extend up to $|\eta| < 3.0$. The HCAL barrel and endcaps similarly cover the region $|\eta| < 3.0$. In addition to the barrel and endcap detectors, CMS has extensive forward calorimetry. Muons are measured in gas-ionization detectors, which are embedded in the steel flux-return yoke outside of the solenoid. The silicon tracker and muon systems play a crucial role in the identification of jets originating from the hadronization of b quarks [14]. Events of interest are selected using a two-tiered trigger system [15]. The first level, composed of custom hardware processors, uses information from the calorimeters and muon detectors to select events at a rate of around 100 kHz within a time interval of less than $4 \mu\text{s}$. The second level, known as the high-level trigger, consists of a farm of processors running a version of the full event reconstruction software optimized for fast processing, and reduces the event rate to less than 1 kHz before data storage. A more detailed description of the CMS detector, together with a definition of the coordinate system used, can be found in Ref. [16].

3 Data sets and event selection

We select dileptonic $t\bar{t}$ events from a data set recorded at $\sqrt{s} = 8$ TeV during 2012 corresponding to an integrated luminosity of $19.7 \pm 0.5 \text{ fb}^{-1}$ [17]. Events are required to pass one of several triggers that require at least two leptons, ee , $e\mu$, or $\mu\mu$, where the leading (higher- p_T) lepton satisfies $p_T > 17$ GeV and the subleading lepton satisfies $p_T > 8$ GeV.

A particle-flow (PF) algorithm [18, 19] is used to reconstruct and identify each individual par-

track in an event by combining information from various subdetectors of CMS. Each event is required to have at least one reconstructed collision vertex, with the primary vertex selected as the one containing the largest $\sum p_T^2$ of associated tracks. Electron candidates are reconstructed by matching a cluster of energy deposits in the ECAL to a reconstructed track [20]. They are required to satisfy $p_T > 20 \text{ GeV}$ and $|\eta| < 2.5$. Muon candidates are reconstructed in a global fit that combines information from the silicon tracker and muon system [21], and must have $p_T > 20 \text{ GeV}$ and $|\eta| < 2.4$. A requirement on the relative isolation is imposed inside a cone $\Delta R = \sqrt{(\Delta\eta)^2 + (\Delta\phi)^2}$ around each lepton candidate, where ϕ is the azimuthal angle in radians. A parameter $I_{\text{rel}} = \sum p_{T_i} / p_T^\ell$ is defined, where the sum includes all reconstructed PF candidates inside the cone (excluding the lepton itself), and p_T^ℓ is the lepton p_T . Electron (muon) candidates are required to have $I_{\text{rel}} < 0.15$ (0.2) with $\Delta R < 0.3$ (0.4). Events selected offline are required to contain exactly two such leptons, ee , $e\mu$, or $\mu\mu$, with opposite charge. For events containing an e^+e^- or $\mu^+\mu^-$ pair, contributions from low-mass resonances are suppressed by requiring an invariant mass of the lepton pair $M_{\ell\ell} > 20 \text{ GeV}$, while contributions from Z boson decays are suppressed by requiring that $|M_Z - M_{\ell\ell}| > 15 \text{ GeV}$, where $M_Z = 91.2 \text{ GeV}$ [22].

Hadronic jets are clustered from PF candidates with the infrared and collinear safe anti- k_T algorithm [23], with a distance parameter R of 0.5, as implemented in the FASTJET package [24]. The jet momentum is determined as the vectorial sum of all particle momenta in this jet. Corrections to the JES and jet energy resolution (JER) are derived using MC simulation, and are confirmed with measurements of the energy balance in quantum chromodynamics (QCD) di-jet, QCD multijet, photon+jet, and Z+jet events [25]. Muons, electrons, and charged hadrons originating from multiple collisions within the same or nearby bunch crossings (pileup), are not included in the jet reconstruction. Contributions from neutral hadrons originating from pileup are estimated and subtracted from the JES. Jets originating from the hadronization of b quarks are identified with a combined secondary vertex (CSV) b tagging algorithm [14], combining information from the jet secondary vertex with the impact parameter significances of its constituent tracks. The algorithm yields a tagging efficiency of approximately 85% and a misidentification rate of 10%. Events are required to contain at least two jets that pass the b tagging algorithm and satisfy $p_T > 30 \text{ GeV}$ and $|\eta| < 2.5$. In this analysis, the two jets satisfying these requirements that have the highest CSV discriminator values are referred to as b jets.

The missing transverse momentum vector is defined as $\vec{p}_T^{\text{miss}} = -\sum \vec{p}_{T_i}$, where the sum includes all reconstructed PF candidates in an event [26]. Its magnitude is referred to as p_T^{miss} . Corrections to the JES and JER are propagated into p_T^{miss} , as well as an offset correction that accounts for pileup interactions. An additional correction mitigates a mild azimuthal dependence, arising from imperfect detector alignment and other effects, which is observed in the reconstructed p_T^{miss} . To further suppress contributions from Drell–Yan processes, events containing an e^+e^- or $\mu^+\mu^-$ pair are required to have $p_T^{\text{miss}} > 40 \text{ GeV}$.

Simulated $t\bar{t}$ signal events are generated with the MADGRAPH 5.1.5.11 matrix-element generator [27], combined with MADSPIN to include spin correlations of the top quark decay products [28], PYTHIA 6.426 with the Z2* tune for parton showering [29], and TAUOLA for the decay of τ leptons [30]. Parton distribution functions (PDFs) are described by the CTEQ6L1 set [31]. The $t\bar{t}$ signal events are generated with seven different values of M_t ranging from 166.5 to 178.5 GeV. The contribution from the W associated single top quark production (tW) is simulated with POWHEG 1.380 [32–35], where the value of M_t is assumed to be 172.5 GeV. Background events from W+jets and Z+jets production are generated with MADGRAPH 5.1.3.30, and contributions from WW, WZ, ZZ processes are simulated with PYTHIA. The CMS detector response to the simulated events is modelled with GEANT4 [36]. All background processes are normalized to

their predicted cross sections [37–41].

With the requirements outlined previously, 41 640 $t\bar{t}$ candidate events are selected in data. The sample composition is estimated in simulation to be 95% dileptonic $t\bar{t}$, 4% single top quark, and 1% other processes including diboson, W +jets, and Drell–Yan production, as well as semileptonic and all-hadronic $t\bar{t}$.

4 Observables

The observables featured in this study have been developed for physics scenarios where undetected particles, such as neutrinos, carry away a portion of the kinematic information necessary for full event reconstruction. In the dileptonic $t\bar{t}$ system, distributions in these observables contain endpoints, edges, and peak regions that are sensitive to the top quark mass. The observables are described in more detail below.

4.1 The $M_{b\ell}$ observable

The $M_{b\ell}$ observable is defined as

$$M_{b\ell} = \sqrt{(p_b + p_\ell)^2}, \quad (1)$$

where p_b and p_ℓ are four-vectors corresponding to a b jet and lepton, respectively. The $b\ell$ pairs underlying each value of $M_{b\ell}$ are chosen out of four possible combinations by an algorithm described below. The $M_{b\ell}$ observable contains a kinematic endpoint that occurs when the b jet and lepton are directly back-to-back in the top quark rest frame. The location of this endpoint, $(M_{b\ell})_{\max}$, is a function of the masses involved in the decay:

$$(M_{b\ell})_{\max} = \frac{\sqrt{(M_t^2 - M_W^2)(M_W^2 - M_\nu^2)}}{M_W}. \quad (2)$$

With $M_t = 172.5$ GeV, $M_W = 80.4$ GeV [22], and $M_\nu = 0$, we have $(M_{b\ell})_{\max} = 152.6$ GeV. Although this endpoint is a theoretical maximum on the value of $M_{b\ell}$ at leading order, events are still observed beyond this value due to background contamination, resolution effects, and nonzero particle widths.

The $M_{b\ell}$ distribution is shown in data and MC simulation in Fig. 1 (left), with a breakdown of signal and background events shown in the simulation. The ‘signal’ category includes $t\bar{t}$ dilepton decays where both b jets are correctly identified by the b tagging algorithm. The background categories include: ‘mistag’ dilepton decays where a light quark or gluon jet is incorrectly selected by the b tagging algorithm; ‘ τ decays’ where dilepton events include at least one τ lepton in the final state subsequently decaying leptonically; and ‘hadronic decays’ that include events where at least one of the top quarks decays hadronically. The ‘non- $t\bar{t}$ bkg’ category consists of single top quark, diboson, W +jets, and Drell–Yan processes. Events in which a top quark decays through a τ lepton contain extra neutrinos stemming from the leptonic τ decay. Although the extra neutrinos cause a small distortion to the kinematic distributions, these events still contribute to the sensitivity of the measurement.

The sensitivity of the $M_{b\ell}$ observable to the value of M_t is demonstrated in Fig. 1 (right), where $M_{b\ell}$ shapes corresponding to three values of the top quark mass in MC simulation (M_t^{MC}) are shown. The variation between these shapes reveals regions of the $M_{b\ell}$ distribution that are sensitive to the value of M_t , such as the edges to the left and right of the $M_{b\ell}$ peak, and regions

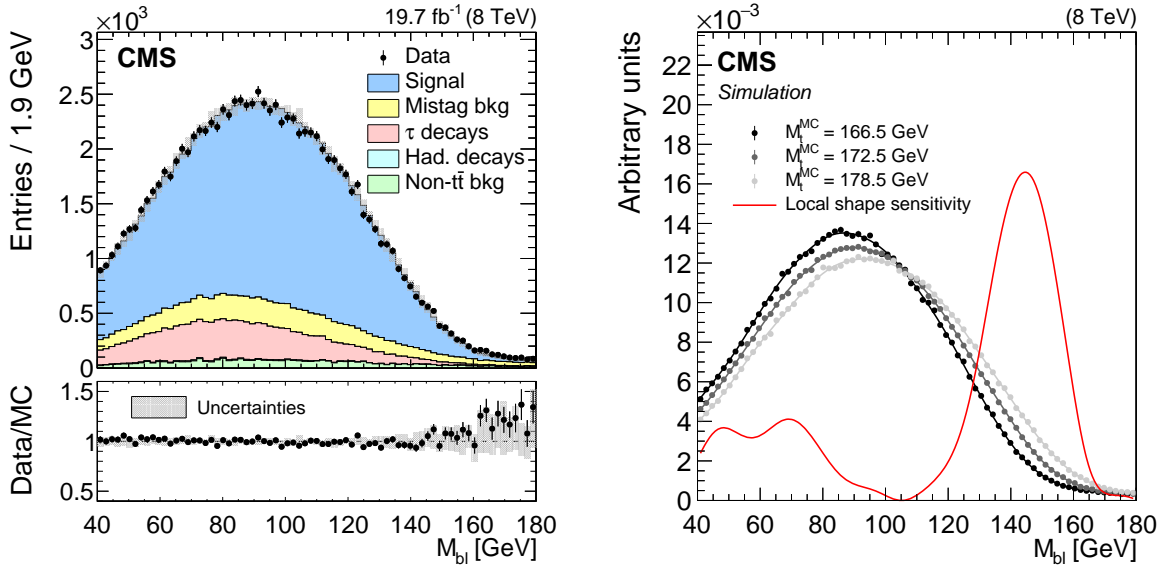


Figure 1: (Left) the $M_{b\ell}$ distribution in data and simulation with $M_t^{\text{MC}} = 172.5$ GeV, normalized to the number of events in the 8 TeV data set corresponding to an integrated luminosity of $19.7 \pm 0.5 \text{ fb}^{-1}$. The lower panel shows the ratio between the data and simulation. Statistical and systematic uncertainties on the distribution in simulation are represented by the shaded area. A description of the systematic uncertainties is given in Section 8. (Right) the $M_{b\ell}$ distribution shapes in simulation, normalized to unit area, corresponding to three values of M_t^{MC} are shown together with the ‘local shape sensitivity’ function, described in Appendix A. The $M_{b\ell}$ distributions include two or three values of $M_{b\ell}$ for each event. The distribution shapes are modeled with a GP regression technique, described in Section 6.

that are not sensitive, such as the stationary point where the three shapes intersect. To provide a quantitative description of these effects, we introduce a ‘local shape sensitivity’ function, also known as the Fisher information density, shown in Figs. 1, 3, and 4. This function conveys the sensitivity of an observable at a specific point on its shape. For the $M_{b\ell}$ observable, the local shape sensitivity function peaks near the kinematic endpoint ($M_{b\ell} \sim 150$ GeV), and has a zero value at the stationary point ($M_{b\ell} \sim 105$ GeV). The integral of this function over its range is proportional to $1/\sigma_{M_t}^2$, where σ_{M_t} is the statistical uncertainty on a measurement of M_t . A full description of the local shape sensitivity function is given in Appendix A.

b jet and lepton combinatorics

The two b jets and two leptons stemming from each $t\bar{t}$ decay give rise to a two-fold matching ambiguity, with two correct and two incorrect $b\ell$ pairings possible in each event. Pairings in which the b jet and lepton emerge from different top quarks do not necessarily obey the upper bound described in Eq. (2), and thus do not have a clean kinematic endpoint in $M_{b\ell}$. Although a priori it is experimentally difficult to distinguish between correct and incorrect pairings, one possible approach is to select the smallest two $M_{b\ell}$ values in each event. This way, the kinematic endpoint of the distribution is preserved – even if the smallest two $M_{b\ell}$ values do not correspond to the correct pairings, they are guaranteed to fall below the correct pairings, which do respect the endpoint. In this analysis, we employ a slightly more sophisticated matching technique, introduced in Ref. [11], where either two or three $b\ell$ pairs are selected in each event.

By selecting either two or three $b\ell$ pairs in each event, the technique employed in this analysis has the benefit of increased statistical power, while preserving the kinematic endpoint of

$M_{b\ell}$. Although they are not necessarily the correct pairs, the corresponding $M_{b\ell}$ values are guaranteed by construction to be less than or equal to those of the correct pairs. The matching technique is based on the following prescription:

1. match each b jet with the lepton that produces the lower $M_{b\ell}$ value;
2. match each lepton with the b jet that produces the lower $M_{b\ell}$ value.

This recipe produces either two or three values of $M_{b\ell}$. In the latter case, two different leptons may be successfully paired with the same b jet, and vice versa. Such a configuration highlights the difference between this recipe and the simpler approach of choosing the smallest two values of $M_{b\ell}$, which do not necessarily incorporate both b jets and both leptons in the event. For example, this could occur if both b jets are matched to a single lepton. In these cases, the next largest $M_{b\ell}$ value is also needed to ensure both b jets and both leptons from the event are used.

4.2 The M_{T2} observable

The M_{T2} ‘stransverse mass’ observable [7, 8] is based on the transverse mass, M_T . The transverse mass of the W boson in a $W \rightarrow \ell\nu$ decay is given by

$$M_T = \sqrt{m_\ell^2 + m_\nu^2 + 2(E_{T\ell}E_{T\nu} - \vec{p}_{T\ell} \cdot \vec{p}_{T\nu})}, \quad (3)$$

where $E_{Tx}^2 = m_x^2 + \vec{p}_T^2$ for $x \in \{\ell, \nu\}$, m_x is the particle mass, and \vec{p}_{Tx} is the particle momentum projected onto the plane perpendicular to the beams. This quantity exhibits a kinematic endpoint at the parent mass, M_W , which occurs in configurations when both the lepton and neutrino momenta lie entirely in the transverse plane (up to a common longitudinal boost).

The dileptonic $t\bar{t}$ system has two layers of decays, with $t \rightarrow Wb$ in the first step followed by $W \rightarrow \ell\nu$ in the second. The result is an event topology with two identical branches, $t \rightarrow b\ell^+\nu$ and $\bar{t} \rightarrow \bar{b}\ell^-\bar{\nu}$, each with a visible ($b\ell$) and invisible (ν) component. In this case, one value of M_T can be computed for each branch. The invisible particle momentum associated with each branch, however, is not known. While for a semileptonic $t\bar{t}$ decay, with only one $W \rightarrow \ell\nu$ decay, the neutrino \vec{p}_T is estimated from the \vec{p}_T^{miss} in the event, a dileptonic $t\bar{t}$ decay includes two neutrinos, for which the allocation of \vec{p}_T^{miss} between them is unknown.

The M_{T2} observable is an extension of M_T for a system with two identical decay branches, ‘a’ and ‘b’, such as those in the dileptonic $t\bar{t}$ system. Here, the invisible particle momenta, \vec{p}_T^a and \vec{p}_T^b , must add up to the total \vec{p}_T^{miss} . The strategy of M_{T2} is to impose this constraint on the invisible particle momenta, while also performing a minimization in order to preserve the kinematic endpoint of M_T . For a general event with a symmetric decay topology, M_{T2} is defined as

$$M_{T2} = \min_{\vec{p}_T^a + \vec{p}_T^b = \vec{p}_T^{\text{miss}}} [\max\{M_T^a, M_T^b\}], \quad (4)$$

where M_T^a and M_T^b correspond to the two decay branches. If the invisible particle mass is known, it can be incorporated into the M_{T2} calculation as well, yielding an endpoint at the parent particle mass. Although the final values of \vec{p}_T^a and \vec{p}_T^b are typically treated as intermediate quantities in the M_{T2} algorithm, they are employed as neutrino \vec{p}_T estimates in the MAOS reconstruction technique described in Section 4.3.

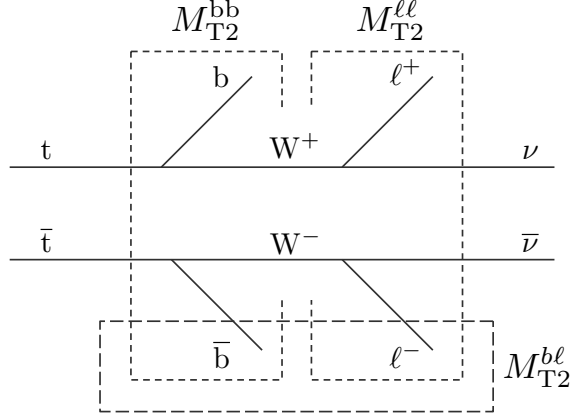


Figure 2: The M_{T2} subsystems in the dileptonic $t\bar{t}$ event topology.

The M_{T2} subsystems

In the $t\bar{t}$ system, there are several ways in which M_{T2} can be computed, depending on how the decay products are grouped together. The M_{T2} algorithm classifies them into three categories: upstream, visible, and child particles [42]. The child particles are those at the end of the decay chain that are unobservable or simply treated as unobservable. In the latter case, the child particle momenta are added to the \vec{p}_T^{miss} vector. The visible particles are those whose \vec{p}_T values are measured and used in the calculations; and the upstream particles are those from further up in the decay chain, including any initial-state radiation (ISR) accompanying the hard collision.

In general, the child, visible, and upstream particles may actually be collections of objects, creating three possible subsystems in the dileptonic $t\bar{t}$ event topology. These subsystems are illustrated in Fig. 2. For simplicity, we refer to the corresponding M_{T2} observables as M_{T2}^{bb} , M_{T2}^{ll} , and M_{T2}^{bl} , where:

- The M_{T2}^{ll} **observable** uses the two leptons as visible particles, treating the neutrinos as invisible child particles, and combining the b jets with all other upstream particles in the event.
- The M_{T2}^{bb} **observable** uses the b jets as visible particles, and treats the W bosons as child particles, ignoring the fact that their charged daughter leptons are indeed observable. It considers only ISR jets as generators of upstream momentum.
- The M_{T2}^{bl} **observable** combines the b jet and the lepton to form a single visible system, and takes the neutrinos as the invisible particles. A two-fold matching ambiguity results from the matching of b jets to leptons in each event. In order to preserve the kinematic endpoint of the M_{T2}^{bl} distribution, the $b\ell$ pair with the smallest value of M_{T2}^{bl} is used in each event.

These observables are identical, respectively, to $M_{T2}^{(2,2,1)}$, $M_{T2}^{(2,1,0)}$, $M_{T2}^{(2,2,0)}$ of Ref. [42], and μ_{bb} , μ_{ll} , μ_{bl} of Ref. [11].

The subsystem observable M_{T2}^{bb} is employed in this study to complement the observable M_{bl} . The M_{T2}^{bb} observable contains an endpoint at the value of M_t , and can be combined with M_{bl} to mitigate uncertainties due to the JES. This feature is discussed further in Section 5. The distribution of M_{T2}^{bb} and its sensitivity to the value of M_t are shown in Fig. 3. Although M_{T2}^{ll} is not directly sensitive to M_t , the neutrino \vec{p}_T estimates that are a by-product of its computation are used as an input into the MAOS $M_{\text{bl}\nu}$ reconstruction technique described in Section 4.3.

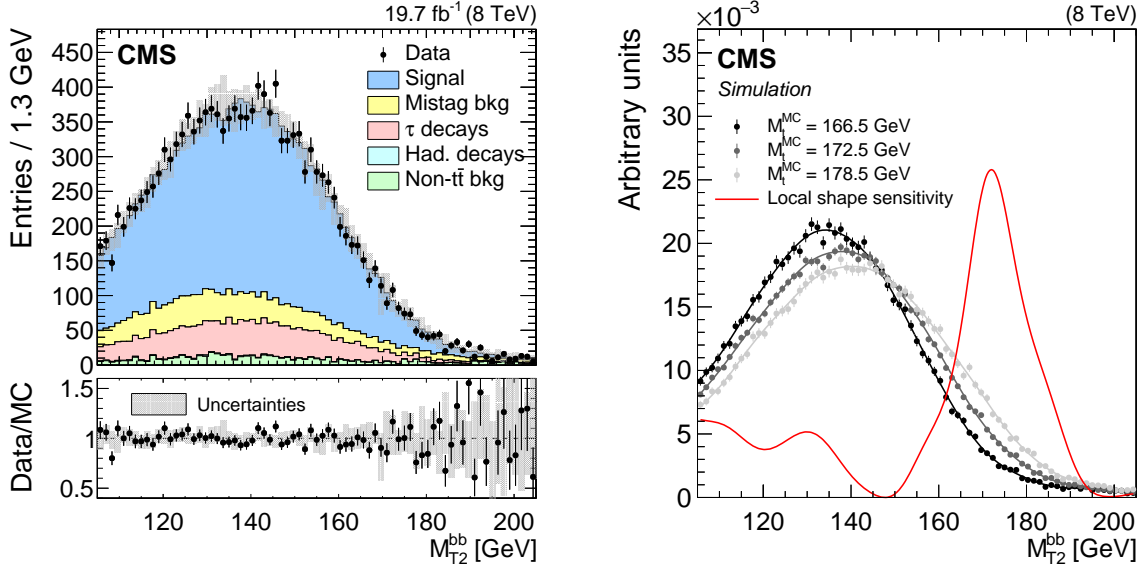


Figure 3: Following the conventions of Fig. 1, shown are the (left) M_{T2}^{bb} distribution in data and simulation with $M_t^{MC} = 172.5$ GeV, and (right) M_{T2}^{bb} distribution shapes in simulation corresponding to three values of M_t^{MC} , along with the ‘local shape sensitivity’ function. The M_{T2}^{bb} distributions include one value of M_{T2}^{bb} for each event if it satisfies the kinematic requirement outlined in Section 4.2.

The M_{T2}^{bb} distribution employed in this analysis includes a kinematic requirement on the upstream momentum, defined as $\vec{p}_T^{\text{upst}} = \sum_{\text{reco}} \vec{p}_{Ti} - \sum_{\text{b jets}} \vec{p}_{Ti} - \sum_{\text{leptons}} \vec{p}_{Ti}$, where the sums are conducted over all reconstructed PF candidates, b jets, and leptons in each event, respectively. The direction of \vec{p}_T^{upst} is required to lie outside the opening angle between the two b jet \vec{p}_T vectors in the event. This requirement primarily impacts events at low values of M_{T2}^{bb} , and its effect on the statistical sensitivity of the observable is small.

4.3 The MAOS $M_{b\ell\nu}$ observable

The MAOS reconstruction technique employed in this analysis is based on the subsystem observable $M_{T2}^{\ell\ell}$. In the $M_{T2}^{\ell\ell}$ algorithm, an M_T variable, defined in Eq. (3), is constructed from the $\ell^+\nu$ and $\ell^-\bar{\nu}$ pairs corresponding to each of the $t\bar{t}$ decay branches. Because the values of neutrino \vec{p}_T are unknown, a minimization is conducted in Eq. (4) over possible values consistent with the measured \vec{p}_T^{miss} in each event.

The MAOS technique employs the neutrino \vec{p}_T values that are determined by the $M_{T2}^{\ell\ell}$ minimization to construct full $b\ell\nu$ invariant mass estimates corresponding to each of the $t\bar{t}$ decay branches. Given the neutrino \vec{p}_T values, the remaining z -components of their momenta are obtained by enforcing the W mass on-shell requirement [22]

$$M(\ell^+\nu) = M(\ell^-\bar{\nu}) = M_W = 80.4 \text{ GeV}. \quad (5)$$

This yields a longitudinal momentum for each neutrino given by

$$p_{zv} = \frac{1}{E_{T\ell}^2} \left[p_{z\ell} A \pm \sqrt{p_{z\ell}^2 + E_{T\ell}^2} \sqrt{A^2 - (E_{T\ell} E_{T\nu})^2} \right], \quad (6)$$

where $A = \frac{1}{2}(M_W^2 + M_\nu^2 + M_\ell^2) + \vec{p}_{T\ell} \cdot \vec{p}_{T\nu}$ [10]. Given these estimates for the neutrino three-momenta together with $M_\nu = 0$, we have the required four vectors to construct an $M_{b\ell\nu}$ invariant mass corresponding to the decay products of each top quark.

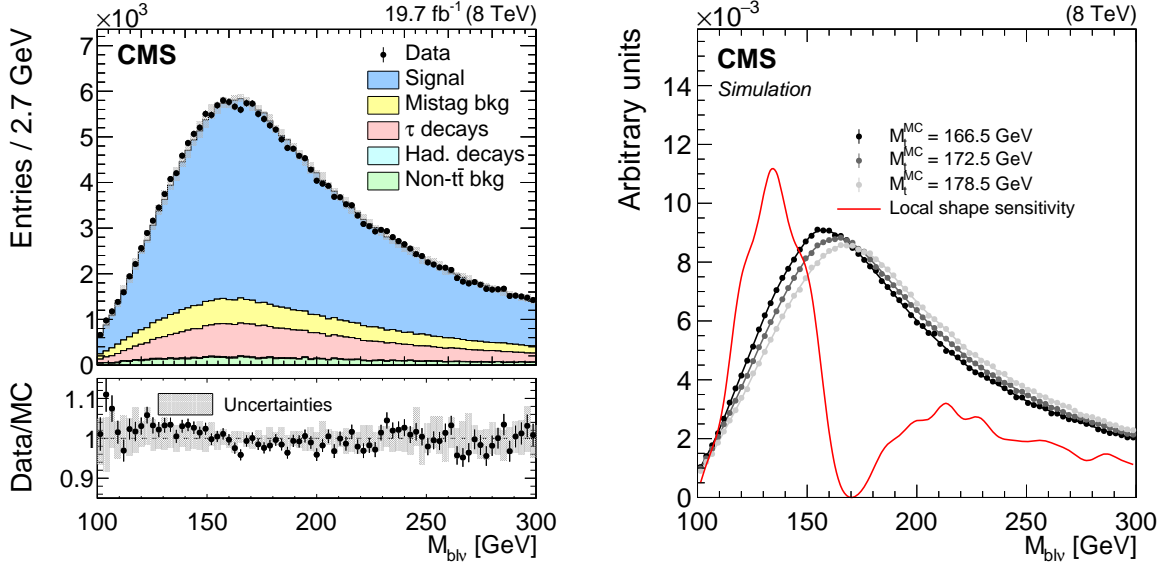


Figure 4: Following the conventions of Fig. 1, shown are the (left) MAOS $M_{b\ell\nu}$ distribution in data and simulation with $M_t^{\text{MC}} = 172.5$ GeV, and (right) the MAOS $M_{b\ell\nu}$ distribution shapes in simulation corresponding to three values of M_t^{MC} , along with the ‘local shape sensitivity’ function. The MAOS $M_{b\ell\nu}$ distributions include up to eight values of $M_{b\ell\nu}$ for each event.

The quadratic equations in Eq. (6) underlying the W mass on-shell requirement provide up to two solutions for each value of $p_{z\nu}$, yielding a two-fold ambiguity for each neutrino momentum. In addition, there is a two-fold ambiguity resulting from the matching of b jets to $\ell\nu$ pairs in the construction of $b\ell\nu$ invariant masses. No matching ambiguity exists between leptons and neutrinos, since the $\ell^+\nu$ and $\ell^-\bar{\nu}$ pairs have been fixed by the $M_{T2}^{\ell\ell}$ algorithm. The combined four-fold ambiguity, along with the two top quark decays in each event, gives up to eight possible values of $M_{b\ell\nu}$. In the measurement, all of the available values are used: for each $\ell\nu$ pair, this includes up to two neutrino $p_{z\nu}$ solutions, and two b - $\ell\nu$ matches. The distribution of MAOS $M_{b\ell\nu}$ and its sensitivity to the value of M_t are shown in Fig. 4.

5 Simultaneous determination of M_t and JSF

To mitigate the impact of JES uncertainties on the precision of this measurement, we introduce a technique that allows a JSF parameter to be fit simultaneously with M_t . The JSF is a constant multiplicative factor that calibrates the overall energy scale of reconstructed jets. It is applied in addition to the standard JES calibration, which corrects the jet response as a function of p_T and η . The dominant component of uncertainty in the JES calibration can be attributed to a global factor in jet response, which is captured in the JSF.

The challenge in determining the JSF simultaneously with M_t stems from the large degree of correlation between these parameters. In the top quark decay, $t \rightarrow b\ell\nu$, the JSF directly affects the momentum of the b jet, and indirectly, the inferred momentum of the neutrino, by scaling all jets entering the p_T^{miss} sum. The M_t parameter affects the momenta of these two particles in addition to the lepton produced in the top quark decay. In the context of observables and distribution shapes, variations in the M_t and JSF parameters cause shape changes that are difficult to distinguish. For this reason, a shape-based analysis using a single observable can be implemented to determine either M_t or JSF, but not both simultaneously.

To determine the M_t and JSF parameters simultaneously, we construct a likelihood function

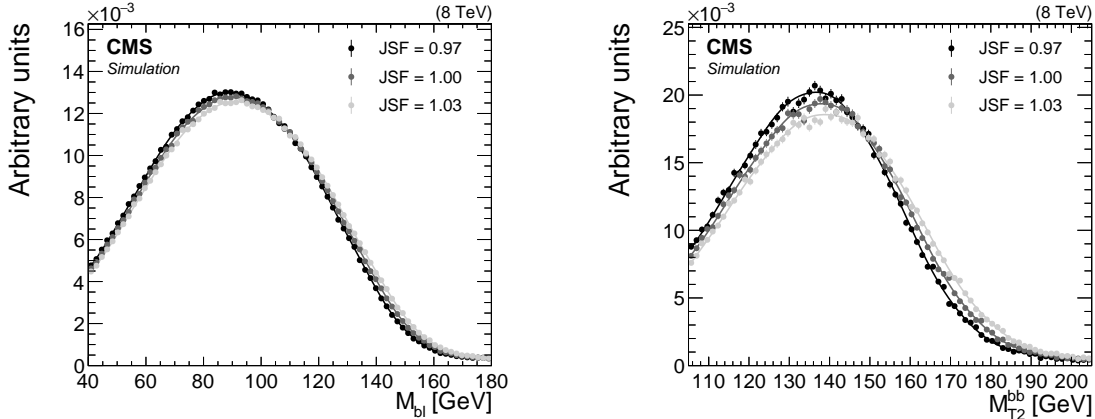


Figure 5: The (left) $M_{b\ell}$ and (right) M_{T2}^{bb} distributions in simulation with $M_t = 172.5$ GeV for several values of JSF. Two or three values are included in the $M_{b\ell}$ distribution for each event, and one value is included in the M_{T2}^{bb} distribution if it satisfies the kinematic requirement outlined in Section 4.2. The distributions are normalized to unit area. The three curves corresponding to each of the $M_{b\ell}$ and M_{T2}^{bb} distributions are obtained using a GP regression technique described in Section 6.

that contains two distributions corresponding to the $M_{b\ell}$ and M_{T2}^{bb} observables. In this configuration, variations in the parameters produce shifts in each individual distribution. They also create a relative shift between the distributions that provides the additional constraint needed for a simultaneous fit of M_t and JSF. The dependence of the $M_{b\ell}$ and M_{T2}^{bb} distribution shapes on M_t is shown in Figs. 1 and 3, and their dependence on the JSF is shown in Fig. 5. The difference in response between the $M_{b\ell}$ and M_{T2}^{bb} shapes to the JSF parameter is rooted in the reconstructed objects underlying the $M_{b\ell}$ and M_{T2}^{bb} observables – while each value of $M_{b\ell}$ uses one b jet and one lepton, each value of M_{T2}^{bb} uses two b jets and no leptons for the visible system. Thus, M_{T2}^{bb} exhibits a stronger dependence on the JSF. The likelihood fit used in this measurement is described in more detail in Section 7.

6 Gaussian processes for shape estimation

In this analysis, the $M_{b\ell}$, M_{T2}^{bb} , and $M_{b\ell\nu}$ distribution shapes are modeled with a GP regression technique that has two main advantages over other commonly-used shape estimate methods. First, the GP shape is nonparametric, determined only by a set of training points and hyperparameters that regulate smoothing; and second, it can be easily trained as a function of several variables simultaneously. The latter feature allows one to capture the smooth evolution of the distribution shapes as the M_t and JSF parameters are varied. A detailed introduction to GPs can be found in Refs. [12, 13]. Here, we give a brief overview of the GP regression technique, with further discussion provided in Appendix B.

The likelihood fit described in Section 7 uses distribution shapes of the form $f(x|M_t, \text{JSF})$, where x is the value of an observable ($M_{b\ell}$, M_{T2}^{bb} , or $M_{b\ell\nu}$), and M_t and JSF are free parameters in the fit. The shapes f are shown in Figs. 1, 3, and 4 for each observable, where the free parameters are set to $M_t = 166.5, 172.5$, or 178.5 GeV and $\text{JSF} = 1$. In Fig. 5, shapes corresponding to the $M_{b\ell}$ and M_{T2}^{bb} observables are shown with the free parameters set to $M_t = 172.5$ GeV and $\text{JSF} = 0.97, 1.00$, or 1.03 . In the figures, these shapes are represented as functions of a single variable (the observable x) with M_t and JSF fixed. In GP regression, however, each shape is treated as a function of all three quantities (x , M_t , and JSF), and can be described as a probabil-

ity density in three dimensions.

Each GP shape is trained using binned distributions of the observable x in MC simulation. For each observable, 35 binned distributions are used, corresponding to seven values of M_t^{MC} ranging from 166.5 to 178.5 GeV and five values of JSF ranging from 0.97 to 1.03. Each distribution has 75 bins in x , yielding a total of 2625 training points at which the value of f is known and used as an input into the GP regression process. Each training point is specified by its values of x , M_t , and JSF. The GP regression technique interpolates between the discrete values of x , M_t , and JSF covered by these training points to provide a shape that is smooth over its range. The smoothness properties of each shape are determined by a kernel function that is set by the analyzer. The GP shapes in this analysis correspond to the kernel function given in Eq. 18 of Appendix B.

The binned distributions used to construct each GP shape are normalized to unity. However, the normalization of the GP shape itself may deviate slightly from unity due to minor imperfections in shape modeling. To mitigate this effect, the GP shape normalization is recomputed for each value of M_t and JSF at which the shape is evaluated. In a likelihood fit, the normalization is recomputed for every variation of the fit parameters.

7 Fit strategy

This measurement employs an unbinned maximum-likelihood fit using the $M_{b\ell}$, M_{T2}^{bb} , and MAOS $M_{b\ell\nu}$ observables described in Section 4, along with the GP shape estimate technique described in Section 6. The MC samples used to train the GP shapes include the $t\bar{t}$ signal and background processes described in Section 3.

The likelihood constructed from a single observable, x , is given by:

$$\mathcal{L}^x(M_t, \text{JSF}) = \prod_i f(x_i | M_t, \text{JSF}). \quad (7)$$

Here, the distribution shape f depends on the value of the free parameters M_t and JSF, and expresses the likelihood of drawing some event i where the value of the observable is x_i . It is normalized to unity over its range for all values of M_t and JSF. The parameters M_t and JSF are varied in the fit to maximize the value of the likelihood.

A likelihood containing two observables, x_1 and x_2 , is constructed as a product of individual likelihoods:

$$\begin{aligned} \mathcal{L}(M_t, \text{JSF}) &= \mathcal{L}^{x_1}(M_t, \text{JSF}) \mathcal{L}^{x_2}(M_t, \text{JSF}) \\ &= \prod_i f(x_{1i} | M_t, \text{JSF}) f(x_{2i} | M_t, \text{JSF}). \end{aligned} \quad (8)$$

This analysis employs three different versions of the likelihood fit:

1. the **1D fit** uses the $M_{b\ell}$ and M_{T2}^{bb} observables to determine M_t , and JSF is constrained to be unity;
2. the **2D fit** also uses $M_{b\ell}$ and M_{T2}^{bb} but imposes no constraint on the JSF and determines M_t and JSF simultaneously;
3. the **MAOS fit** uses the M_{T2}^{bb} and $M_{b\ell\nu}$ observables to determine M_t , and JSF is constrained to be unity.

Among these versions, the 1D fit provides the best precision on the value of M_t . The 2D fit mitigates the JES uncertainties, which are the largest source of systematic error in the 1D approach. The MAOS fit is expected to yield results similar to the 1D fit, and is presented as a viable alternative that substitutes the $M_{b\ell}$ observable for MAOS $M_{b\ell\nu}$. The best overall precision on M_t is given by a combination of the 1D and 2D fits, which is discussed below. The fit results are discussed in Section 9.

The central value and statistical uncertainty on M_t and JSF are determined using the bootstrapping technique [43]. This method is based on pseudo-experiments rather than the shape of the total likelihood defined in Eq. (8) near its maximum, and thus mitigates the effects of correlation between the two observables, x_1 and x_2 , in the likelihood. The technique also mitigates possible correlations within the $M_{b\ell}$ and $M_{b\ell\nu}$ observables when multiple values of the observable occur in a single event. The bootstrapping technique is primarily relevant for statistical uncertainty determination, which may otherwise be affected by correlations in the likelihood. The technique has a negligible impact on the central values of M_t and JSF. The bootstrap pseudo-experiments are constructed by resampling the full data set with replacement, where the size of each pseudo-experiment is fixed to have the number of events in data (41 640 events). Events are selected at random from the full data set, so that a particular event has the same probability of being chosen at any stage during the sampling process. In this procedure, a single event may be selected more than once for any given pseudo-experiment. In data, all events have an equal probability to be selected. In simulation, the probability of selecting a particular event is proportional to its weight, containing the relevant cross sections, as well as corrections for MC modeling and object reconstruction efficiencies.

The performance of the likelihood fitting approach described above is evaluated using events in simulation, where the true values of M_t and JSF are known. The fit is conducted using seven different values of M_t^{MC} ranging from 166.5 to 178.5 GeV for each version of the likelihood fit. The results of this performance study are shown in Fig. 6. The likelihood fits are consistent with zero bias, showing that the GP shape modeling technique accurately captures the distribution shapes and their evolution over several values of M_t^{MC} . For this reason, no calibration of the fit is necessary for an unbiased determination of the M_t and JSF parameters.

Combination of 1D and 2D fits

The 1D and 2D fits discussed above have differing sensitivities to various sources of systematic uncertainty in this measurement. Although the 2D fit successfully mitigates the JES uncertainties, which dominate in the 1D fit, other uncertainties in the 2D method are larger and cause the total precision to worsen (Section 8). The best overall precision on the value of M_t is provided by a **hybrid fit**, defined as a linear combination of the 1D and 2D fits. The measured value of M_t in the hybrid fit is given by:

$$M_t^{\text{hyb}} = w_{\text{hyb}} M_t^{\text{1D}} + (1 - w_{\text{hyb}}) M_t^{\text{2D}}, \quad (9)$$

where the parameter w_{hyb} determines the relative weight between the 1D and 2D fits in the combination. The value of M_t^{hyb} and its statistical uncertainty are extracted using bootstrap pseudo-experiments, as described above. In each pseudo-experiment, the measured value of M_t^{hyb} is given by the linear combination in Eq. (9) of the measured M_t^{1D} and M_t^{2D} values. A value of $w_{\text{hyb}} = 0.8$ is found to achieve the best precision on M_t when both statistical and systematic uncertainties are taken into account. The performance of the hybrid fit, evaluated using MC samples corresponding to seven values of M_t^{MC} , is shown in Fig. 6.

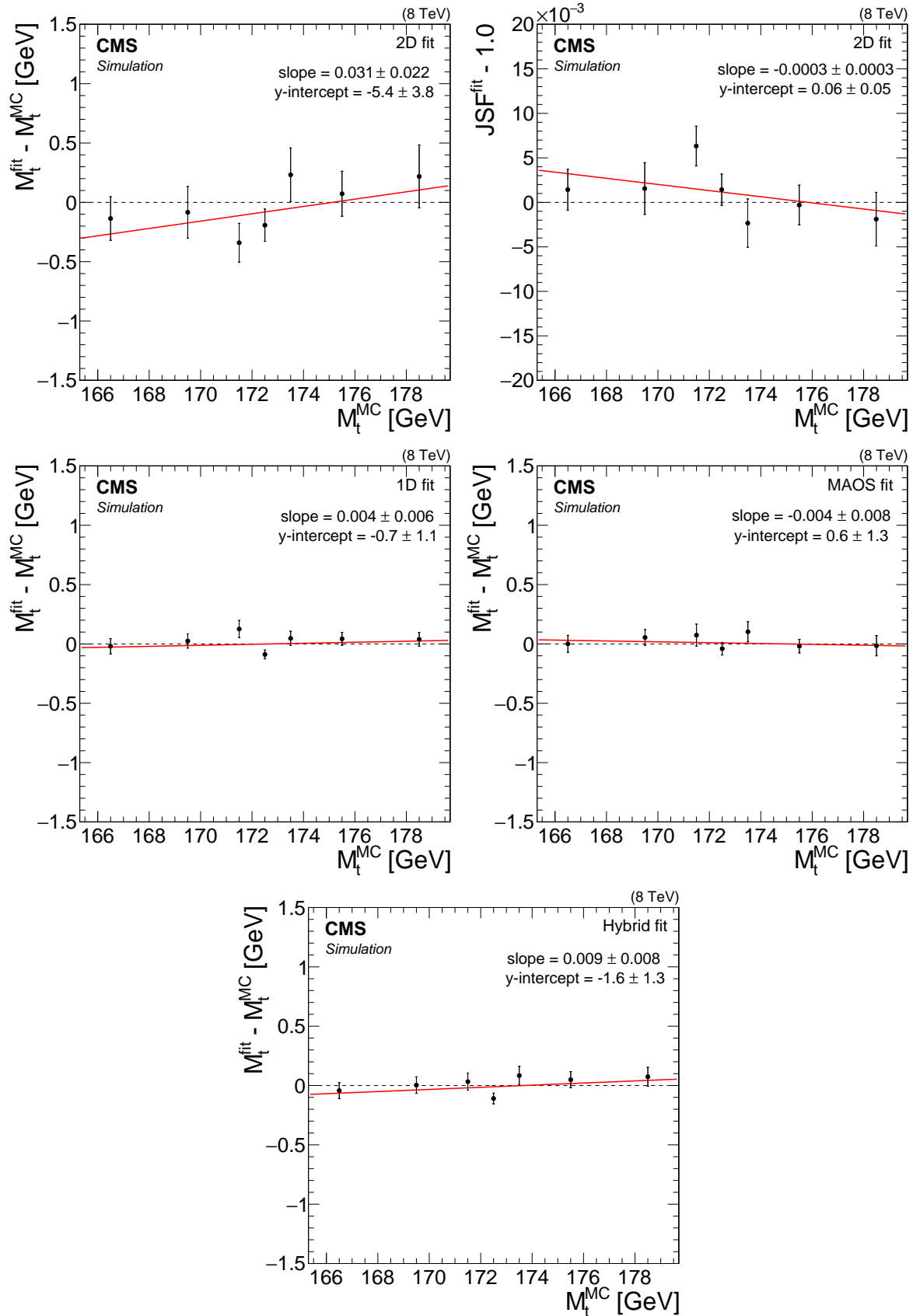


Figure 6: Likelihood fit results as a function of M_t^{MC} corresponding to the (top) 2D, (center left) 1D, (center right) MAOS, and (bottom) hybrid fits. For each value of M_t^{MC} , the fit is conducted using 50 pseudo-experiments in MC simulation. The mean parameter values, M_t^{fit} and JSF^{fit} , are represented by the points, with statistical uncertainties indicated by the error bars. A best-fit line of the form $y = ax + b$ is shown for each fit configuration.

8 Systematic uncertainties

The systematic uncertainties evaluated in this measurement are given in Table 1. The uncertainties include experimental effects from detector calibration and object reconstruction, and modeling effects mostly arising from the simulation of QCD processes. All uncertainties are determined by conducting the likelihood fit using events from MC simulation with the relevant parameters varied by $\pm 1\Delta$, where Δ is the uncertainty on a particular parameter. The difference in the measured top quark mass (δM_t) or JSF (δJSF) is taken to be the corresponding systematic uncertainty. For uncertainties that are evaluated by comparing two or more independent MC samples, the values of δM_t and δJSF may be subject to statistical fluctuations. For this reason, if the value of δM_t or δJSF is smaller than its statistical uncertainty in a particular systematic variation, the statistical uncertainty is quoted as the systematic uncertainty. Finally, if a systematic uncertainty is one-sided, where both $+\Delta$ and $-\Delta$ variations produce δM_t or δJSF shifts of the same sign, the larger shift is taken as the symmetric systematic uncertainty.

In the hybrid fit, the systematic uncertainties are evaluated according to the linear combination in Eq. (9). For each systematic variation, this gives $\delta M_t^{\text{hyb}} = w_{\text{hyb}} \delta M_t^{\text{1D}} + (1 - w_{\text{hyb}}) \delta M_t^{\text{2D}}$. This approach provides the smallest overall uncertainty, with the largest contributions stemming from the JES, b quark fragmentation modeling, and hard scattering scale. The next most precise result is given by the 1D fit, also dominated by the same sources of uncertainty. The JES uncertainties are successfully mitigated in the 2D fit. The 2D fit, however, is more sensitive to the uncertainties in the top quark p_T spectrum, matching scale, and underlying event tune, so the total systematic uncertainty for the 2D fit is larger than that of the 1D fit. The MAOS fit has a larger total systematic uncertainty than the 1D fit due to its sensitivity to the JES, top quark p_T spectrum, and b quark fragmentation modeling uncertainties. Further details on each source of systematic uncertainty are given below.

- Jet energy scale: The JES uncertainty is evaluated separately for four components, which are then added in quadrature [44]. The ‘Intercalibration’ uncertainty arises from the modeling of radiation in the p_T - and η -dependent JES determination. The ‘In situ’ category includes uncertainties stemming from the determination of the absolute JES using γ/Z -jet events. The ‘Uncorrelated’ uncertainty includes uncertainties due to detector effects and pileup. Finally, the ‘Flavor’ uncertainty stems from differences in the energy response between different jet flavors – it is a linear sum of contributions from the light quark, charm quark, bottom quark, and gluon responses, which are estimated by comparing the Lund string fragmentation in PYTHIA [29] and cluster fragmentation in HERWIG++ [45] for each type of jet. All JES uncertainties are propagated into the reconstructed p_T^{miss} in each event.
- b quark fragmentation: The b quark fragmentation uncertainty includes two components that are implemented using event weights. The first component stems from the b quark fragmentation function, which can be modeled using the Lund fragmentation model in the PYTHIA Z2* tune, or tuned to empirical results from the ALEPH [46] and DELPHI [47] experiments. This component is evaluated by comparing the measurement results in MC simulation using these two tunes of the b quark fragmentation function, with the difference symmetrized to obtain the corresponding uncertainty. The second uncertainty component stems from the B hadron semileptonic branching fraction, which has an impact on the b quark JES due to the production of a neutrino. The corresponding uncertainty is evaluated by repeating the measurement with branching fraction values of 10.05% and 11.27%, which are variations about the nominal value of 10.50% and encompass the range of values measured

Table 1: Systematic uncertainties for the 2D, 1D, hybrid, and MAOS likelihood fits. The breakdown of JES and b quark fragmentation uncertainties into separate components is shown, where the components are added in quadrature to obtain the total. The ‘up’ and ‘down’ variations are given separately, with the sign of each variation indicating the direction of the corresponding shift in M_t or JSF. The \otimes character highlights the uncertainty sources that are large in at least one of the likelihood fits.

		δM_t^{2D}	δJSF^{2D}	δM_t^{1D}	δM_t^{hyb}	δM_t^{MAOS}
		[GeV]		[GeV]	[GeV]	[GeV]
JES (total)	\otimes	+0.06 −0.10	+0.007 −0.006	+0.54 −0.55	+0.43 −0.46	+0.65 −0.70
– In situ		+0.04 −0.04	−0.002 +0.003	−0.22 +0.21	−0.18 +0.17	−0.28 +0.24
– Intercalibration		−0.01 +0.01	<0.001 <0.001	−0.04 +0.03	−0.03 +0.03	−0.04 +0.04
– Uncorrelated		+0.04 −0.04	−0.005 +0.005	−0.39 +0.39	−0.32 +0.31	−0.47 +0.47
– Flavor		+0.02 −0.09	+0.004 −0.003	+0.31 −0.32	+0.25 −0.27	+0.39 −0.43
b quark frag. (total)	\otimes	+0.39 −0.39	+0.001 −0.001	+0.40 −0.40	+0.40 −0.40	+0.67 −0.67
– Frag. function		+0.38 −0.38	<0.001 <0.001	+0.38 −0.38	+0.38 −0.38	+0.64 −0.64
– Branching fraction		+0.07 −0.07	+0.001 −0.001	+0.13 −0.13	+0.12 −0.12	+0.20 −0.20
JER		−0.03 +0.08	+0.001 −0.002	+0.01 −0.05	<0.00 −0.03	+0.04 −0.04
Unclustered energy		+0.10 −0.10	+0.001 −0.001	−0.02 +0.02	−0.04 +0.01	−0.11 +0.12
Pileup		−0.06 +0.04	<0.001 <0.001	−0.06 +0.05	−0.06 +0.05	−0.06 +0.05
Electron energy scale		−0.38 +0.39	+0.002 −0.003	−0.21 +0.21	−0.24 +0.24	−0.02 +0.05
Muon momentum scale		−0.11 +0.09	+0.001 <0.001	−0.06 +0.05	−0.07 +0.06	<0.01 +0.01
Electron Id/Iso		+0.07 −0.02	−0.001 <0.001	+0.03 −0.01	+0.03 −0.01	+0.01 <0.01
Muon Id/Iso		<0.01 <0.01	<0.001 <0.001	<0.01 <0.01	<0.01 <0.01	<0.01 <0.01
b tagging		+0.03 −0.03	<0.001 −0.001	−0.01 +0.01	<0.01 <0.01	<0.01 <0.01
Top quark p_T reweighting	\otimes	+0.93 —	−0.007 —	+0.40 —	+0.51 —	+0.72 —
Hard scattering scale	\otimes	−0.36 +0.20	+0.007 −0.003	+0.31 −0.49	+0.21 −0.47	+0.33 −0.08
Matching scale	\otimes	−0.86 +0.30	−0.004 +0.008	−0.25 +0.11	−0.37 +0.12	+0.12 −0.12
Underlying event tunes	\otimes	+0.56 −0.56	+0.007 −0.007	+0.08 −0.08	+0.11 −0.11	+0.09 −0.09
Color reconnection		+0.06 −0.06	+0.001 −0.001	+0.15 −0.15	+0.13 −0.13	+0.16 −0.16
ME Generator		+0.18 −0.18	−0.004 +0.002	−0.19 +0.07	−0.13 +0.07	+0.11 −0.07
PDFs		+0.14 −0.14	+0.001 −0.001	+0.17 −0.16	+0.17 −0.15	+0.17 −0.16
Total		+1.31 −1.25	+0.015 −0.014	+0.91 −0.95	+0.89 −0.93	+1.27 −1.02

from B hadron decays and their uncertainties [22]. Both uncertainty components are combined in quadrature to obtain the total uncertainty.

- **Jet energy resolution:** The energy resolution of jets is known to be underestimated in MC simulation compared to data. This effect is corrected with a set of scale factors that are used to smear the jet four-vectors to broaden their resolutions. The scale factors are determined in bins of η . Here, they are varied within their uncertainties, which are typically 2.5–5%. The effect of these variations is also propagated into the p_T^{miss} .
- **Unclustered energy:** The unclustered energy in each event comprises the low- p_T hadronic activity that is not clustered into a jet. Here, the scale of the unclustered energy is varied by $\pm 10\%$ [26].
- **Pileup:** The uncertainty in the number of pileup interactions in MC simulation stems from the instantaneous luminosity in each bunch crossing and the effective inelastic cross section. In this analysis, the number of pileup interactions in MC is reweighted to match the data. The pileup uncertainty is evaluated by varying the effective inelastic cross section by $\pm 5\%$.
- **Lepton energy scale:** The electron energy scale is varied up and down by 0.6% in the ECAL barrel ($|\eta| < 1.48$) and by 1.5% in the ECAL endcap ($1.48 < |\eta| < 3.0$) [20]. The muon momentum scale is varied up and down by 0.2%. All variations are propagated into the p_T^{miss} .
- **Lepton identification and isolation:** Event weights are applied to adjust the electron and muon yields in MC simulation to account for differences in the identification and isolation efficiencies between data and simulation. For muons, the uncertainty is taken to be 0.5% of the identification event weight, and 0.2% of the isolation event weight [21]. For electrons, the uncertainties are estimated in bins of p_T and η , and are approximately 0.1–0.5% of the combined event weight for identification and isolation [20].
- **b tagging efficiency:** Event weights are applied to adjust the b jet yields in MC simulation to account for the difference in the b tagging efficiency between data and MC simulation [14]. The uncertainties are evaluated in bins of p_T and η .
- **Top quark p_T reweighting:** Event weights are applied in order to compensate for a difference in the top quark p_T spectrum between data and MC simulation [48]. The uncertainty is evaluated by comparing the measurement in MC simulation with and without the weights applied. The event weights are not applied in the nominal result. This uncertainty is one-sided by construction, and is not symmetrized.
- **Hard scattering scale:** The factorization scale, μ_F , determines the threshold separating the parton-parton hard scattering from softer interactions embodied in the PDFs. The renormalization scale, μ_R , sets the energy scale at which matrix-element calculations are evaluated. Both of these scales are set to $\mu_F = \mu_R = Q$ in the matrix-element calculation and the initial-state parton shower of the MADGRAPH samples, where $Q^2 = M_t^2 + \sum p_T^2$. Here, the sum runs over all additional final state partons in the matrix element. The values of μ_F and μ_R are varied simultaneously up and down by a factor of two to estimate the corresponding uncertainty.
- **Matching scale:** The matrix element-parton shower matching threshold is used to interface the matrix elements generated in MADGRAPH with parton showers simulated in PYTHIA. Its reference value of 20 GeV is varied up and down by a factor of two.

- Underlying event tunes and color reconnection: The underlying event tunes affect the modeling of soft hadronic activity that results from beam remnants and multiparton interactions in each event. The measurement is conducted with a $t\bar{t}$ sample from MC simulation using the ‘Perugia 2011’ tune. It is compared to results using samples with the ‘Perugia 2011 mpiHi’ and ‘Perugia 2011 Tevatron’ tunes [49] in PYTHIA, corresponding to an increased and decreased underlying event activity, respectively. The largest difference is symmetrized to obtain the final uncertainty. The color reconnection (CR) uncertainty is evaluated by comparing measurement results using $t\bar{t}$ samples with the ‘Perugia 2011’ and ‘Perugia 2011 no CR’ tunes [49], where CR effects are not included in the latter. The difference is symmetrized to obtain the final uncertainty.
- Matrix-element generator: The measurement is repeated using MC samples produced with the POWHEG event generator, which provides a next-to-leading-order calculation of the $t\bar{t}$ production. These measurement results are compared with the reference $t\bar{t}$ MC sample, generated using MADGRAPH, to determine the corresponding uncertainty.
- Parton distribution functions: Initial-state partons are described by PDFs. The corresponding uncertainty is evaluated by applying event weights in the MC simulation to reflect the CT10 PDF set [50] with 50 error eigenvectors. The total PDF uncertainty is determined by adding the variations corresponding to these error sets in quadrature.

9 Results and discussion

The results for each version of the likelihood fit, determined from 1000 bootstrap pseudo-experiments in each fit, are shown in Fig. 7. The 2D fit uses the $M_{b\ell}$ and M_{T2}^{bb} observables to simultaneously determine the values of M_t and JSF, yielding $M_t^{2D} = 171.56 \pm 0.46$ (stat) $^{+1.31}_{-1.25}$ (syst) GeV and $\text{JSF}^{2D} = 1.011 \pm 0.006$ (stat) $^{+0.015}_{-0.014}$ (syst). The correlation between the M_t and JSF fit parameters in the 2D fit is shown in Fig. 8, with a correlation coefficient of $\rho = -0.94$. The $M_{b\ell}$ and M_{T2}^{bb} distribution shapes corresponding to the fit results in a typical pseudo-experiment are shown in Fig. 9. The 2D fit is successful in mitigating the uncertainty due to the determination of JES, which is otherwise the largest source of systematic uncertainty in this measurement. In particular, this approach is insensitive to the flavor-dependent component of JES uncertainties — stemming from differences in the response between b jets, light-quark jets, and gluon jets — since predominantly b jets are used for the determination of both M_t and JSF parameters. The underlying strategy, rooted in a simultaneous fit of two distributions with differing sensitivities to the JSF, does not rely on any specific assumptions about the event topology or final state. For this reason, it can be a viable option for JES uncertainty mitigation in a variety of physics scenarios.

The 1D fit is also based on the $M_{b\ell}$ and M_{T2}^{bb} observables, but constrains the JSF parameter to unity. The 1D fit gives a value of $M_t^{1D} = 172.39 \pm 0.17$ (stat) $^{+0.91}_{-0.95}$ (syst) GeV. In this approach, the JES accounts for the largest source of uncertainty. However, other uncertainties are reduced with respect to the 2D fit, resulting in an improved overall precision.

The best overall precision is given by the hybrid fit, which is given by a linear combination of the 1D and 2D fit results. The 1D and 2D fits use the same set of events and an identical likelihood function constructed from the $M_{b\ell}$ and M_{T2}^{bb} observables. These fits are fully correlated, with the only difference between them stemming from the treatment of the JSF pa-

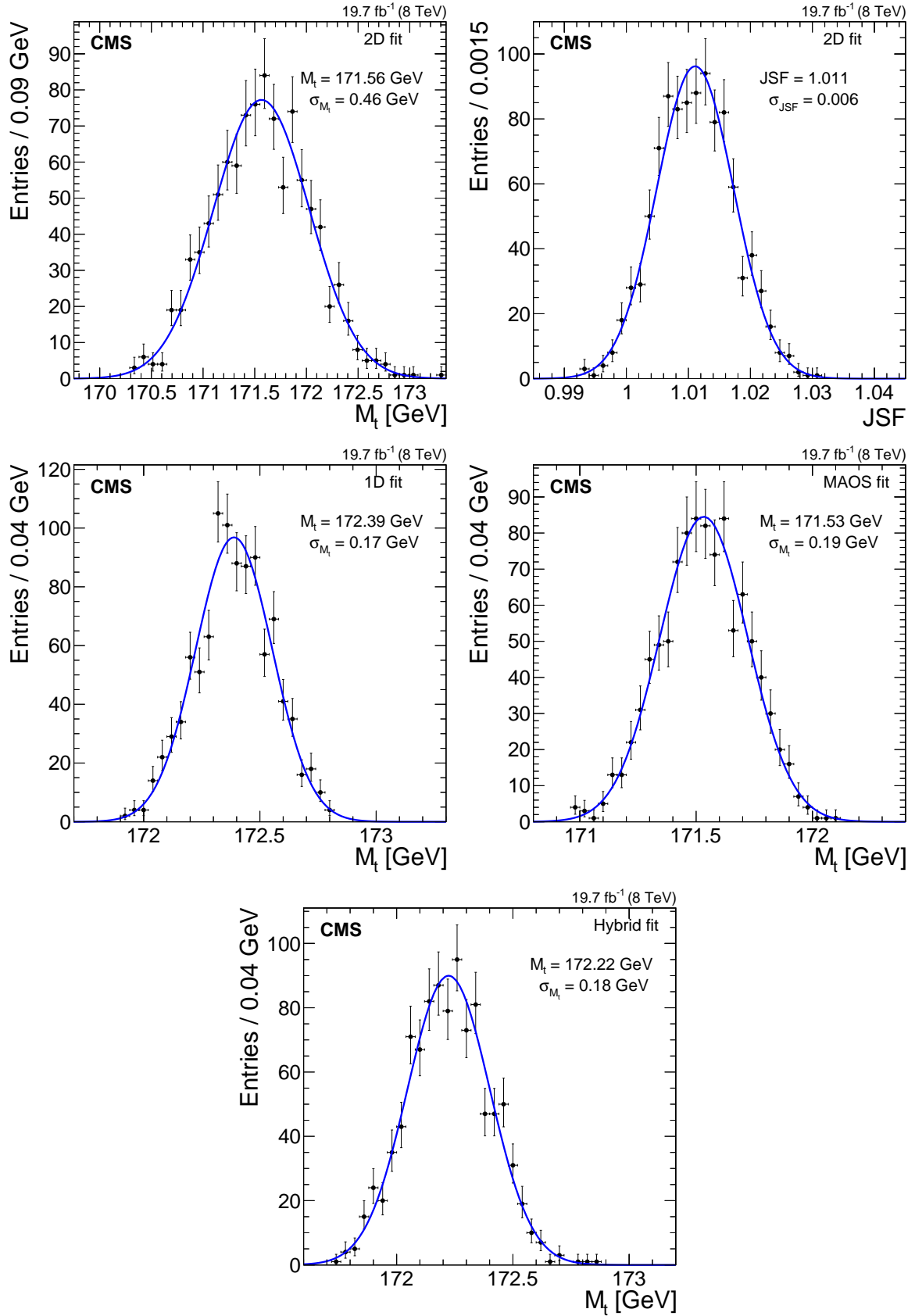


Figure 7: Likelihood fit results using 1000 bootstrap pseudo-experiments for the (top) 2D fit, (center left) 1D fit, and (center right) MAOS fit. (Bottom) hybrid fit results given by the linear combination in Eq. (9) of the 1D and 2D fits. The error bars represent the statistical uncertainty corresponding to the number of pseudo-experiments in each bin.

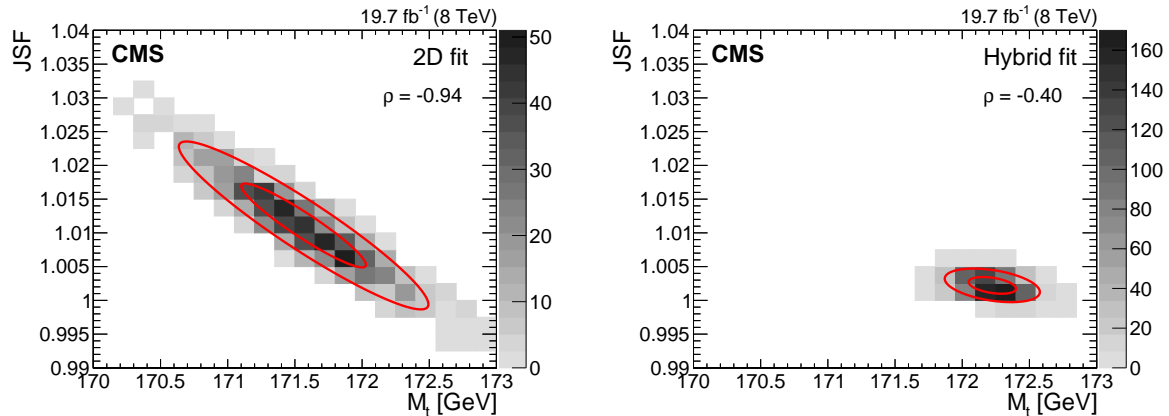


Figure 8: Likelihood fit results corresponding to the 2D fit (left) and hybrid fit (right), obtained using 1000 pseudo-experiments constructed with the bootstrapping technique. The shaded histogram represents the number of pseudo-experiments in each bin of M_t and JSF. Two-dimensional contours corresponding to $-\Delta \log(\mathcal{L}) = 1(4)$ are shown, allowing the construction of one (two) σ statistical intervals in M_t and JSF. The hybrid fit results are given by a linear combination of the 1D and 2D fit results using Eq. (9).

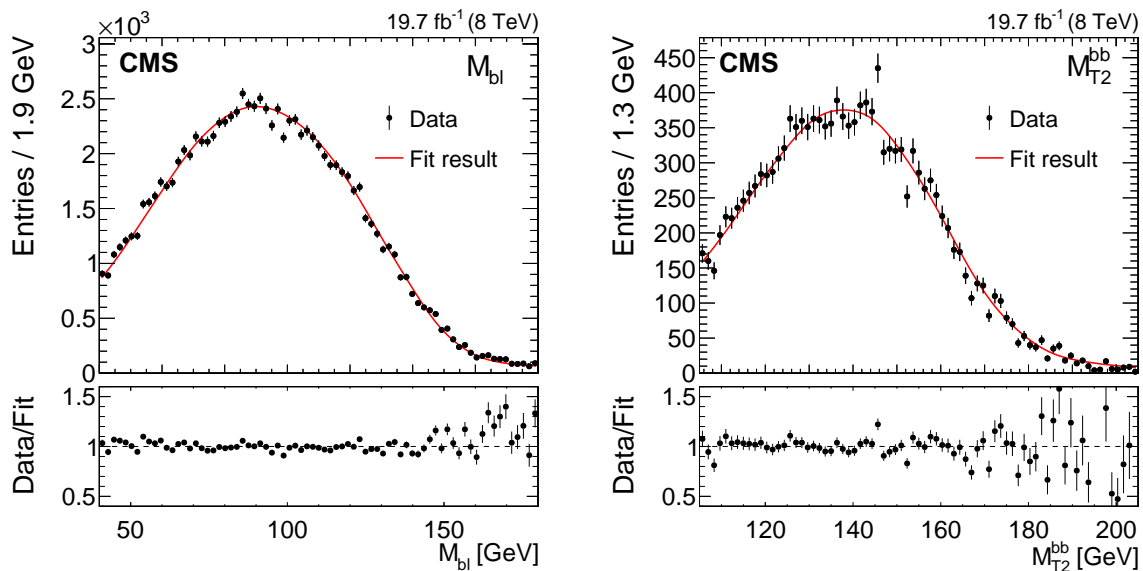


Figure 9: Maximum-likelihood fit result in a typical pseudo-experiment of the 2D likelihood fit in data. The best fit parameter values for this pseudo-experiment are $M_t = 171.99$ GeV and $JSF = 1.007$. When the JSF parameter is constrained to be unity in the 1D likelihood fit, the best fit value of M_t is 172.48 GeV. The lower panel shows the ratio between the distribution in data and the best fit distribution in simulation.

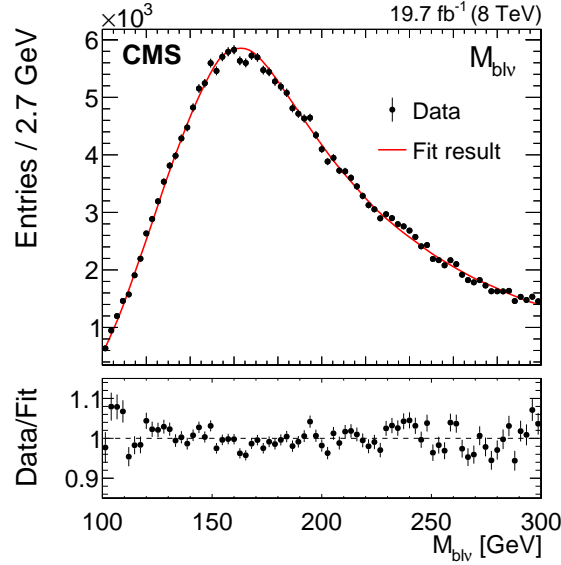


Figure 10: The MAOS $M_{b\ell\nu}$ distribution corresponding to the maximum-likelihood fit result in a typical pseudo-experiment of the MAOS likelihood fit in data. The best fit value of M_t for this pseudo-experiment is 171.54 GeV. The lower panel shows the ratio between the distribution in data and the best fit distribution in simulation.

parameter, which is fixed to unity in the 1D fit and acts as a free parameter in the 2D fit. The choice to fix the JSF parameter or allow it to float has an impact on the fit sensitivity to a variety of uncertainty sources in addition to the JES. A linear combination of the 1D and 2D fits with $w_{\text{hyb}} = 0.8$, as defined in Eq. (9), achieves an optimal balance between all uncertainty sources, thus providing the best overall precision. The hybrid fit gives:

$$M_t^{\text{hyb}} = 172.22 \pm 0.18 \text{ (stat)}_{-0.93}^{+0.89} \text{ (syst)} \text{ GeV}.$$

The correlation between the M_t and JSF fit parameters in the hybrid fit is shown in Fig. 8, with a correlation coefficient of $\rho = -0.40$.

The MAOS fit substitutes the $M_{b\ell}$ observable for an $M_{b\ell\nu}$ invariant mass, yielding a value of $M_t^{\text{MAOS}} = 171.54 \pm 0.19 \text{ (stat)}_{-1.02}^{+1.27} \text{ (syst)} \text{ GeV}$. The MAOS observable presents a new approach for mass reconstruction in a decay topology characterized by underconstrained kinematics. Here, the MAOS fit provides a determination of M_t that is complementary to the 2D, 1D, and hybrid fits. The MAOS $M_{b\ell\nu}$ distribution shape corresponding to the fit results in a typical pseudo-experiment is shown in Fig. 10. The results for each version of the likelihood fit are summarized in Fig. 11.

10 Summary

A measurement of the top quark mass (M_t) in the dileptonic $t\bar{t}$ decay channel is performed using proton-proton collisions at $\sqrt{s} = 8 \text{ TeV}$, corresponding to an integrated luminosity of $19.7 \pm 0.5 \text{ fb}^{-1}$. The measurement is based on the mass observables $M_{b\ell}$, M_{T2}^{bb} , and $M_{b\ell\nu}$, which allow for mass reconstruction in decay topologies that are kinematically underconstrained. The sensitivity of these observables to the value of M_t is investigated using a Fisher information density technique. The observables are employed in three versions of an unbinned likelihood fit, where a Gaussian process technique is used to model the corresponding distribution shapes and their evolution in M_t and an overall jet energy scale factor (JSF). The Gaussian process

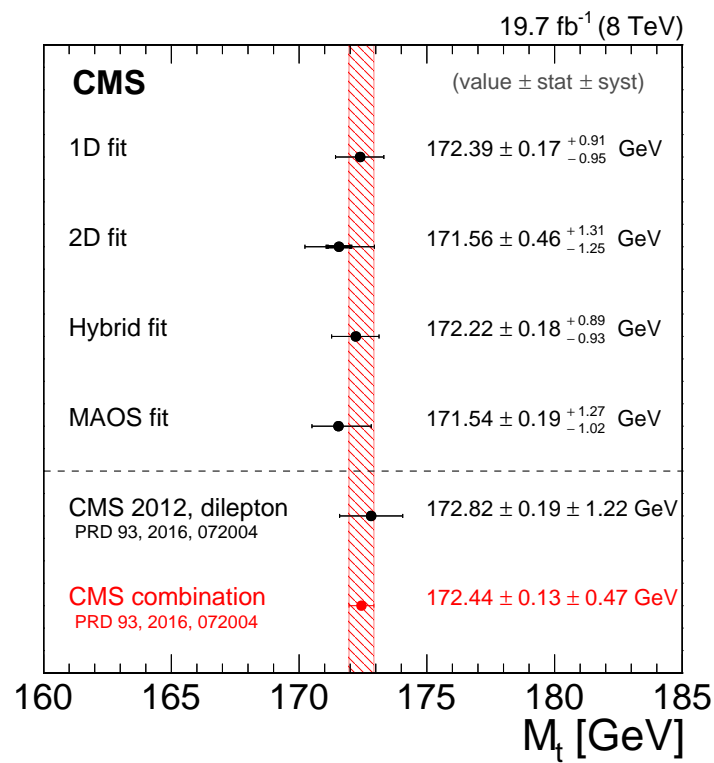


Figure 11: Summary of the 1D, 2D, hybrid, and MAOS likelihood fit results using the 2012 data set at $\sqrt{s} = 8$ TeV, corresponding to an integrated luminosity of 19.7 ± 0.5 fb⁻¹. A recent dileptonic channel measurement using the 2012 dataset and the most recent combination of M_t measurements by CMS in all $t\bar{t}$ decay channels [5] are shown below the dashed line for reference.

shapes are nonparametric, and allow for a likelihood fitting framework that gives unbiased results. The 2D fit provides the first simultaneous measurement of M_t and JSF in the dileptonic channel. It is robust against uncertainties due to the determination of jet energy scale, including the flavor-dependent uncertainty component arising from differences in the response between b jets, light-quark jets, and gluon jets. The fit yields $M_t = 171.56 \pm 0.46$ (stat) $^{+1.31}_{-1.25}$ (syst) GeV and JSF = 1.011 ± 0.006 (stat) $^{+0.015}_{-0.014}$ (syst). The most precise measurement of M_t is given by a linear combination of this result with a fit in which the JSF is constrained to be unity, yielding a value of 172.22 ± 0.18 (stat) $^{+0.89}_{-0.93}$ (syst) GeV. This measurement achieves a 25% improvement in overall precision on M_t compared to previous dileptonic channel analyses using the 2012 data set at CMS. The improvement can be attributed to a reduction of the systematic uncertainties in the measurement.

Acknowledgments

We congratulate our colleagues in the CERN accelerator departments for the excellent performance of the LHC and thank the technical and administrative staffs at CERN and at other CMS institutes for their contributions to the success of the CMS effort. In addition, we gratefully acknowledge the computing centers and personnel of the Worldwide LHC Computing Grid for delivering so effectively the computing infrastructure essential to our analyses. Finally, we acknowledge the enduring support for the construction and operation of the LHC and the CMS detector provided by the following funding agencies: BMWFW and FWF (Austria); FNRS and FWO (Belgium); CNPq, CAPES, FAPERJ, and FAPESP (Brazil); MES (Bulgaria); CERN; CAS, MoST, and NSFC (China); COLCIENCIAS (Colombia); MSES and CSF (Croatia); RPF (Cyprus); SENESCYT (Ecuador); MoER, ERC IUT, and ERDF (Estonia); Academy of Finland, MEC, and HIP (Finland); CEA and CNRS/IN2P3 (France); BMBF, DFG, and HGF (Germany); GSRT (Greece); OTKA and NIH (Hungary); DAE and DST (India); IPM (Iran); SFI (Ireland); INFN (Italy); MSIP and NRF (Republic of Korea); LAS (Lithuania); MOE and UM (Malaysia); BUAP, CINVESTAV, CONACYT, LNS, SEP, and UASLP-FAI (Mexico); MBIE (New Zealand); PAEC (Pakistan); MSHE and NSC (Poland); FCT (Portugal); JINR (Dubna); MON, RosAtom, RAS, RFBR and RAEP (Russia); MESTD (Serbia); SEIDI, CPAN, PCTI and FEDER (Spain); Swiss Funding Agencies (Switzerland); MST (Taipei); ThEPCenter, IPST, STAR, and NSTDA (Thailand); TUBITAK and TAEK (Turkey); NASU and SFFR (Ukraine); STFC (United Kingdom); DOE and NSF (USA). If acknowledgements for individuals are required for a short letter because some of the principal authors are funded through individual grants, it should be OK to add the lines below concerning individuals even for a short letter, but please first consult with the PubComm chair.

Individuals have received support from the Marie-Curie program and the European Research Council and EPLANET (European Union); the Leventis Foundation; the A. P. Sloan Foundation; the Alexander von Humboldt Foundation; the Belgian Federal Science Policy Office; the Fonds pour la Formation à la Recherche dans l'Industrie et dans l'Agriculture (FRIA-Belgium); the Agentschap voor Innovatie door Wetenschap en Technologie (IWT-Belgium); the Ministry of Education, Youth and Sports (MEYS) of the Czech Republic; the Council of Science and Industrial Research, India; the HOMING PLUS program of the Foundation for Polish Science, cofinanced from European Union, Regional Development Fund, the Mobility Plus program of the Ministry of Science and Higher Education, the National Science Center (Poland), contracts Harmonia 2014/14/M/ST2/00428, Opus 2014/13/B/ST2/02543, 2014/15/B/ST2/03998, and 2015/19/B/ST2/02861, Sonata-bis 2012/07/E/ST2/01406; the National Priorities Research Program by Qatar National Research Fund; the Programa Clarín-COFUND del Principado de

Asturias; the Thalys and Aristeia programs cofinanced by EU-ESF and the Greek NSRF; the Rachadapisek Sompot Fund for Postdoctoral Fellowship, Chulalongkorn University and the Chulalongkorn Academic into Its 2nd Century Project Advancement Project (Thailand); and the Welch Foundation, contract C-1845.

References

- [1] Gfitter Group, “The global electroweak fit at NNLO and prospects for the LHC and ILC”, *Eur. Phys. J. C* **74** (2014) 3046, doi:10.1140/epjc/s10052-014-3046-5, arXiv:1407.3792.
- [2] G. Degrandi et al., “Higgs mass and vacuum stability in the Standard Model at NNLO”, *JHEP* **08** (2012) 098, doi:10.1007/JHEP08(2012)098, arXiv:1205.6497.
- [3] A. H. Hoang and I. W. Stewart, “Top Mass Measurements from Jets and the Tevatron Top-Quark Mass”, *Nucl. Phys. Proc. Suppl.* **185** (2008) 220, doi:10.1016/j.nuclphysbps.2008.10.028, arXiv:0808.0222.
- [4] ATLAS, CDF, CMS, and D0 Collaborations, “First combination of Tevatron and LHC measurements of the top-quark mass”, (2014). arXiv:1403.4427.
- [5] CMS Collaboration, “Measurement of the top quark mass using proton-proton data at $\sqrt{s} = 7$ and 8 TeV”, *Phys. Rev. D* **93** (2016) 072004, doi:10.1103/PhysRevD.93.072004, arXiv:1509.04044.
- [6] ATLAS Collaboration, “Measurement of the top quark mass in the $t\bar{t} \rightarrow$ dilepton channel from $\sqrt{s} = 8$ TeV ATLAS data”, *Phys. Lett. B* **761** (2016) 350, doi:10.1016/j.physletb.2016.08.042, arXiv:1606.02179.
- [7] A. J. Barr and C. G. Lester, “A review of the mass measurement techniques proposed for the Large Hadron Collider”, *J. Phys. G* **37** (2010) 123001, doi:10.1088/0954-3899/37/12/123001, arXiv:1004.2732.
- [8] C. G. Lester and D. J. Summers, “Measuring masses of semi-invisibly decaying particle pairs produced at hadron colliders”, *Phys. Lett. B* **463** (1999) 99, doi:10.1016/S0370-2693(99)00945-4, arXiv:hep-ph/9906349.
- [9] H.-C. Cheng and Z. Han, “Minimal kinematic constraints and M_{T2} ”, *JHEP* **12** (2008) 063, doi:10.1088/1126-6708/2008/12/063, arXiv:0810.5178.
- [10] W. S. Cho, K. Choi, Y. G. Kim, and C. B. Park, “ M_{T2} -assisted on-shell reconstruction of missing momenta and its application to spin measurement at the LHC”, *Phys. Rev. D* **79** (2009) 031701, doi:10.1103/PhysRevD.79.031701, arXiv:0810.4853.
- [11] CMS Collaboration, “Measurement of masses in the $t\bar{t}$ system by kinematic endpoints in pp collisions at $\sqrt{s} = 7$ TeV”, *Eur. Phys. J. C* **73** (2013) 2494, doi:10.1140/epjc/s10052-013-2494-7, arXiv:1304.5783.
- [12] C. E. Rasmussen and C. K. I. Williams, “Gaussian Processes for Machine Learning”. MIT Press, 2006. ISBN 026218253X.
- [13] C. Bishop, “Pattern recognition and machine learning”. Springer-Verlag, New York, 1 edition, 2006. ISBN 9780387310732.

- [14] CMS Collaboration, "Identification of b-quark jets with the CMS experiment", *JINST* **8** (2013) P04013, doi:10.1088/1748-0221/8/04/P04013, arXiv:1211.4462.
- [15] CMS Collaboration, "The CMS trigger system", *JINST* **12** (2017) P01020, doi:10.1088/1748-0221/12/01/P01020, arXiv:1609.02366.
- [16] CMS Collaboration, "The CMS experiment at the CERN LHC", *JINST* **3** (2008) S08004, doi:10.1088/1748-0221/3/08/S08004.
- [17] CMS Collaboration, "CMS Luminosity Based on Pixel Cluster Counting - Summer 2013 Update", CMS Physics Analysis Summary CMS-PAS-LUM-13-001, 2013.
- [18] CMS Collaboration, "Particle-Flow Event Reconstruction in CMS and Performance for Jets, Taus, and p_T^{miss} ", CMS Physics Analysis Summary CMS-PAS-PFT-09-001, 2009.
- [19] CMS Collaboration, "Commissioning of the Particle-flow Event Reconstruction with the first LHC collisions recorded in the CMS detector", CMS Physics Analysis Summary CMS-PAS-PFT-10-001, 2010.
- [20] CMS Collaboration, "Performance of electron reconstruction and selection with the CMS detector in proton-proton collisions at $\sqrt{s} = 8$ TeV", *JINST* **10** (2015) P06005, doi:10.1088/1748-0221/10/06/P06005, arXiv:1502.02701.
- [21] CMS Collaboration, "Performance of CMS muon reconstruction in pp collision events at $\sqrt{s} = 7$ TeV", *JINST* **7** (2012) P10002, doi:10.1088/1748-0221/7/10/P10002, arXiv:1206.4071.
- [22] Particle Data Group, C. Patrignani et al., "Review of particle physics", *Chin. Phys. C* **40** (2016) 100001, doi:10.1088/1674-1137/40/10/100001.
- [23] M. Cacciari, G. P. Salam, and G. Soyez, "The anti- k_t jet clustering algorithm", *JHEP* **04** (2008) 063, doi:10.1088/1126-6708/2008/04/063, arXiv:0802.1189.
- [24] M. Cacciari, G. P. Salam, and G. Soyez, "FastJet user manual", *Eur. Phys. J. C* **72** (2012) 1896, doi:10.1140/epjc/s10052-012-1896-2, arXiv:1111.6097.
- [25] CMS Collaboration, "Jet energy scale and resolution in the CMS experiment in pp collisions at 8 TeV", *JINST* **12** (2017) P02014, doi:10.1088/1748-0221/12/02/P02014, arXiv:1607.03663.
- [26] CMS Collaboration, "Performance of the CMS missing transverse momentum reconstruction in pp data at $\sqrt{s} = 8$ TeV", *JINST* **10** (2015) P02006, doi:10.1088/1748-0221/10/02/P02006, arXiv:1411.0511.
- [27] J. Alwall et al., "The automated computation of tree-level and next-to-leading order differential cross sections, and their matching to parton shower simulations", *JHEP* **07** (2014) 079, doi:10.1007/JHEP07(2014)079, arXiv:1405.0301.
- [28] P. Artoisenet, R. Frederix, O. Mattelaer, and R. Rietkerk, "Automatic spin-entangled decays of heavy resonances in Monte Carlo simulations", *JHEP* **03** (2013) 015, doi:10.1007/JHEP03(2013)015, arXiv:1212.3460.
- [29] T. Sjöstrand, S. Mrenna, and P. Skands, "PYTHIA 6.4 physics and manual", *JHEP* **05** (2006) 026, doi:10.1088/1126-6708/2006/05/026, arXiv:hep-ph/0603175.

- [30] S. Jadach, Z. Was, R. Decker, and J. H. Kuhn, “The tau decay library TAUOLA: Version 2.4”, *Comput. Phys. Commun.* **76** (1993) 361, doi:10.1016/0010-4655(93)90061-G.
- [31] W.-K. Tung, “New Generation of Parton Distributions with Uncertainties from Global QCD Analysis”, *Acta Phys. Polon. B* **33** (2002) 2933, arXiv:hep-ph/0206114.
- [32] S. Alioli, P. Nason, C. Oleari, and E. Re, “NLO single-top production matched with shower in POWHEG: s - and t -channel contributions”, *JHEP* **09** (2009) 111, doi:10.1088/1126-6708/2009/09/111, arXiv:0907.4076. [Erratum: doi:10.1007/JHEP02(2010)011].
- [33] E. Re, “Single-top Wt -channel production matched with parton showers using the POWHEG method”, *Eur. Phys. J. C* **71** (2011) 1547, doi:10.1140/epjc/s10052-011-1547-z, arXiv:1009.2450.
- [34] S. Frixione, P. Nason, and C. Oleari, “Matching NLO QCD computations with Parton Shower simulations: the POWHEG method”, *JHEP* **11** (2007) 070, doi:10.1088/1126-6708/2007/11/070, arXiv:0709.2092.
- [35] S. Alioli, P. Nason, C. Oleari, and E. Re, “A general framework for implementing NLO calculations in shower Monte Carlo programs: the POWHEG BOX”, *JHEP* **06** (2010) 043, doi:10.1007/JHEP06(2010)043, arXiv:1002.2581.
- [36] GEANT4 Collaboration, “GEANT4—a simulation toolkit”, *Nucl. Instrum. Meth. A* **506** (2003) 250, doi:10.1016/S0168-9002(03)01368-8.
- [37] N. Kidonakis, “Next-to-next-to-leading soft-gluon corrections for the top quark cross section and transverse momentum distribution”, *Phys. Rev. D* **82** (2010) 114030, doi:10.1103/PhysRevD.82.114030, arXiv:1009.4935.
- [38] N. Kidonakis, “Differential and total cross sections for top pair and single top production”, in *Proceedings, 20th International Workshop on Deep-Inelastic Scattering and Related Subjects (DIS 2012)*, p. 831. Bonn, Germany, 2012. arXiv:1205.3453. doi:10.3204/DESY-PROC-2012-02/251.
- [39] K. Melnikov and F. Petriello, “Electroweak gauge boson production at hadron colliders through $O(\alpha_s^2)$ ”, *Phys. Rev. D* **74** (2006) 114017, doi:10.1103/PhysRevD.74.114017, arXiv:hep-ph/0609070.
- [40] J. M. Campbell and R. K. Ellis, “MCFM for the Tevatron and the LHC”, *Nucl. Phys. Proc. Suppl.* **205-206** (2010) 10, doi:10.1016/j.nuclphysbps.2010.08.011, arXiv:1007.3492.
- [41] M. Czakon, P. Fiedler, and A. Mitov, “Total top-quark pair-production cross section at hadron colliders through $O(\alpha_s^4)$ ”, *Phys. Rev. Lett.* **110** (2013) 252004, doi:10.1103/PhysRevLett.110.252004, arXiv:1303.6254.
- [42] M. Burns, K. Kong, K. T. Matchev, and M. Park, “Using subsystem M_{T2} for complete mass determinations in decay chains with missing energy at hadron colliders”, *JHEP* **03** (2009) 143, doi:10.1088/1126-6708/2009/03/143, arXiv:0810.5576.
- [43] B. Efron and R. Tibshirani, “An Introduction to the Bootstrap”. Monographs on Statistics and Applied Probability. Chapman & Hall, 1993.

- [44] CMS and ATLAS Collaborations, “Jet energy scale uncertainty correlations between ATLAS and CMS at 8 TeV”, CMS Physics Analysis Summary CMS-PAS-JME-15-001, ATL-PHYS-PUB-2015-049, 2015.
- [45] M. Bähr et al., “Herwig++ physics and manual”, *Eur. Phys. J. C* **58** (2008) 639, doi:10.1140/epjc/s10052-008-0798-9, arXiv:0803.0883.
- [46] ALEPH Collaboration, “Study of the fragmentation of b quarks into B mesons at the Z peak”, *Phys. Lett. B* **512** (2001) 30, doi:10.1016/S0370-2693(01)00690-6, arXiv:hep-ex/0106051.
- [47] DELPHI Collaboration, “A study of the b-quark fragmentation function with the DELPHI detector at LEP I and an averaged distribution obtained at the Z Pole”, *Eur. Phys. J. C* **71** (2011) 1557, doi:10.1140/epjc/s10052-011-1557-x, arXiv:1102.4748.
- [48] CMS Collaboration, “Measurement of the differential cross section for top quark pair production in pp collisions at $\sqrt{s} = 8$ TeV”, *Eur. Phys. J. C* **75** (2015) 542, doi:10.1140/epjc/s10052-015-3709-x, arXiv:1505.04480.
- [49] P. Z. Skands, “Tuning Monte Carlo generators: the Perugia tunes”, *Phys. Rev. D* **82** (2010) 074018, doi:10.1103/PhysRevD.82.074018, arXiv:1005.3457.
- [50] H.-L. Lai et al., “New parton distributions for collider physics”, *Phys. Rev. D* **82** (2010) 074024, doi:10.1103/PhysRevD.82.074024, arXiv:1007.2241.
- [51] H. Crámer, “Mathematical Methods of Statistics”. Princeton University Press, 1999. ISBN 9780691005478.
- [52] A. DasGupta, “Asymptotic Theory of Statistics and Probability”. Springer, 2008. ISBN 9780387759708. doi:10.1007/978-0-387-75971-5.

A Statistical sensitivity of kinematic observables

The sensitivity of a kinematic observable to the value of a parameter such as M_t can be quantified by its Fisher information [51, 52]. The Fisher information of an observable is related to its likelihood function, \mathcal{L} , which we have introduced in Eq. (7) and reproduce here:

$$\log \mathcal{L}(m) = \sum_i^N \log f(x_i|m), \quad (10)$$

where $f(x|m)$ is the distribution of observable x normalized to unity over its range, m is a free parameter, and N is the number of observations of x . In this measurement, we have $x = M_{b\ell}$, M_{T2}^{bb} , or $M_{b\ell\nu}$, $m = M_t$ or JSF, and N is a multiple of the total number of events. For simplicity we consider the distribution shape f as a function of only one free parameter. The Fisher information corresponding to the shape $f(x|m)$ is given by:

$$\mathcal{I}(m) = \int \left(\frac{\partial}{\partial m} \log f(x|m) \right)^2 f(x|m) dx. \quad (11)$$

The quantity $\mathcal{I}(m)$ provides a measure of curvature near the likelihood maximum. It can be interpreted as the variance of the slope, $(\partial \log f(x|m)/\partial m)$, known as the ‘statistical score’ of $f(x|m)$.

The Fisher information is related to the precision of a measurement by the Crámer-Rao bound:

$$\sigma_m^2 \geq \frac{1}{N\mathcal{I}(m)}, \quad (12)$$

where σ_m is the statistical uncertainty on parameter m . In a likelihood with large N , the shape of the likelihood near its maximum is roughly Gaussian, and the bound approaches an equality. This expression confirms the expected relationship $\sigma_m \propto 1/\sqrt{N}$ between the statistical uncertainty and the value of N , but also reveals the proportionality factor as the reciprocal of the Fisher information. It expresses the uncertainty σ_m in terms of the total number of events, the shape f , and the derivative $\partial f/\partial m$.

The Fisher information also provides a mathematical framework for quantifying the sensitivity of an observable at a specific point on its shape. In this analysis, the $M_{b\ell}$ and M_{T2}^{bb} observables have kinematic endpoints at approximately $\sqrt{M_t^2 - M_W^2}$ and M_t , respectively; the MAOS $M_{b\ell\nu}$ observable is an invariant mass whose shape contains a peak near the value of M_t . Because these features carry a dependence on the value of M_t , the regions near the endpoints of $M_{b\ell}$ and M_{T2}^{bb} and the peak of $M_{b\ell\nu}$ are expected to contribute significantly to the sensitivity of these observables. To relate these local features to the Fisher information, we consider the integral in Eq. (11) over the value of observable x . Here, the integrand of the Fisher information can be interpreted as the contribution to the total sensitivity stemming from a specific value of x . Rewriting the integrand in a more convenient form, we define the ‘local shape sensitivity’ function by:

$$s(x|m) \equiv \frac{1}{f(x|m)} \left[\frac{\partial f(x|m)}{\partial m} \right]^2. \quad (13)$$

This function is also known as the Fisher information density. It is shown for the $M_{b\ell}$, M_{T2}^{bb} , and MAOS $M_{b\ell\nu}$ observables in Figs. 1, 3, and 4, respectively, with $m = M_t$ and the JSF parameter fixed to unity. It is observed to peak near the kinematic endpoints of $M_{b\ell}$ and M_{T2}^{bb} , and on the left-side edge of $M_{b\ell\nu}$. The values of x where $s(x|m) = 0$ coincide with the stationary points at

which the distribution shapes in Figs. 1, 3, and 4 intersect. This is a reflection of the fact that in a likelihood fit, events with a value of x near a stationary point make little or no contribution to the determination of m . In general, the shape of $s(x|m)$ for each observable establishes a link between the underlying kinematic properties of the observable and regions of high and low sensitivity on its shape. In this analysis, it provides heuristic information about the $M_{b\ell}$, M_{T2}^{bb} , and MAOS $M_{b\ell\nu}$ distributions, and their sensitivity to the value of M_t .

In addition to providing heuristic information, the local shape sensitivity function is used in this analysis to identify potential overfitting effects in the Gaussian process (GP) shapes. Overfitting occurs when the interpolation between GP training points is not smooth, causing fluctuations in the shape that may be difficult to identify by eye. Such fluctuations can be a source of bias, both in the determination of M_t and its corresponding uncertainties. A typical symptom of overfitting is an under-estimated statistical uncertainty on the value of M_t . This can occur when fluctuations in the GP shape increase the value of the slope $\partial f(x|M_t)/\partial M_t$ appearing in Eq. (11), thus artificially increasing the Fisher information of the corresponding shape. The issue is easily revealed by the shape of $s(x|M_t)$, which acquires visible fluctuations when overfitting is indeed present. In such cases, overfitting can be mitigated by increasing relevant GP hyperparameter values to improve the smoothness of the GP shape.

B Gaussian process regression technique

The likelihood fit described in Section 7 uses distribution shapes of the form $f(x|M_t, \text{JSF})$, where x is the value of an observable ($M_{b\ell}$, M_{T2}^{bb} , or $M_{b\ell\nu}$), and M_t and JSF are free parameters in the fit. In this analysis, the distribution shapes f are modeled with a Gaussian process (GP) regression technique. We define a point, \mathbf{u}_i , on each distribution shape by its position in x , M_t , and JSF:

$$\mathbf{u}_i \equiv (x_i, M_{ti}, \text{JSF}_i). \quad (14)$$

The value of the shape at \mathbf{u}_i is given by $f(\mathbf{u}_i) = f(x_i|M_{ti}, \text{JSF}_i)$. The point \mathbf{u}_i can be a training point, at which the value of f is known and used as an input into the GP regression process; or it can be a test point, at which the value of f is to be determined. Each GP shape is trained using binned distributions of the observable x in MC simulation. For each observable, 35 binned distributions are used, corresponding to seven values of M_t^{MC} ranging from 166.5 to 178.5 GeV and five values of JSF ranging from 0.97 to 1.03. Each distribution has 75 bins in x , yielding a total of 2625 training points. This binning scheme is chosen to provide an accurate modeling of the distribution shapes, while mitigating the effects of statistical fluctuations. The GP regression technique interpolates between the discrete values of x , M_t , and JSF covered by these training points to provide a shape that is smooth over its range.

The ‘Gaussian’ in GP refers to the distribution of possible values of the shape f . The value at a single point, $f(\mathbf{u}_i)$, is distributed according to a one-dimensional Gaussian function rather than being treated as an exact quantity. The mean of this Gaussian function is the most probable value of the shape at that point \mathbf{u}_i , and it is the value used for likelihood fitting (Section 7); the variance stems from the modeling uncertainty inherent in the GP regression process. The values $f(\mathbf{u}_i)$ and $f(\mathbf{u}_j)$ at any two points follow a two-dimensional Gaussian distribution and are related by a covariance. The correlation between $f(\mathbf{u}_i)$ and $f(\mathbf{u}_j)$ determines the degree to which the GP shape is allowed to vary between the points \mathbf{u}_i and \mathbf{u}_j . By extension, any N values of the shape are described by an N -dimensional Gaussian distribution, and are related by an $N \times N$ covariance matrix. To determine the value of the shape at a test point \mathbf{u}_{N+1} , an $(N+1)$ -dimensional Gaussian distribution is constructed relating the training point values $f(\mathbf{u}_1) \dots f(\mathbf{u}_N)$ to the test point value $f(\mathbf{u}_{N+1})$. Then, $f(\mathbf{u}_1) \dots f(\mathbf{u}_N)$ are fixed to their known

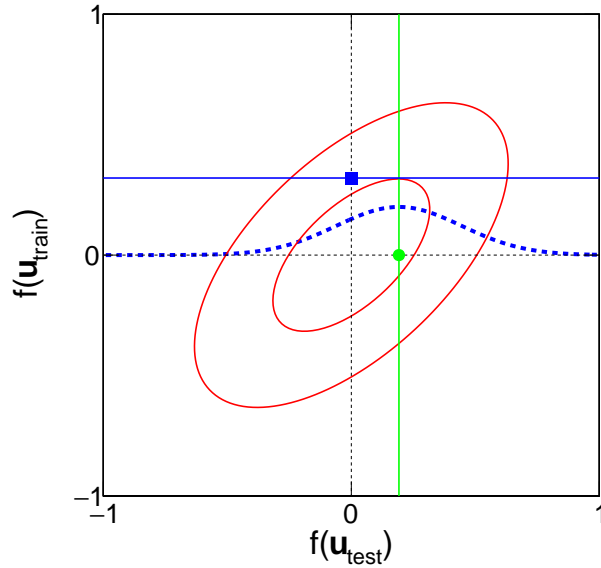


Figure 12: Demonstration of the GP conditioning process, given in Eqs. (16) and (17), for one training point and one test point. The covariance between the value of the shape at the training and test point is represented by the ellipse. The known value of the shape at the training point (square point) determines the mean value of the shape at the test point (round point and vertical line). The distribution of possible values of the shape at the test point is represented by the dashed curve.

values, and the $(N + 1)$ -dimensional Gaussian distribution is reduced to a one-dimensional conditional Gaussian distribution representing the possible values of $f(\mathbf{u}_{N+1})$.

To demonstrate this process graphically, we consider a simple GP with one training point, $\mathbf{u}_{\text{train}}$, at which the value $f(\mathbf{u}_{\text{train}})$ is known, and one test point, \mathbf{u}_{test} , at which the value $f(\mathbf{u}_{\text{test}})$ is to be evaluated. The values of $f(\mathbf{u}_{\text{train}})$ and $f(\mathbf{u}_{\text{test}})$ follow a two-dimensional Gaussian prior distribution with mean values μ_{train} and μ_{test} , and a covariance represented by:

$$\mathbf{C} = \begin{bmatrix} \sigma_{\text{train}}^2 & \rho\sigma_{\text{train}}\sigma_{\text{test}} \\ \rho\sigma_{\text{train}}\sigma_{\text{test}} & \sigma_{\text{test}}^2 \end{bmatrix}, \quad (15)$$

where σ_{train}^2 and σ_{test}^2 are the variances of $f(\mathbf{u}_{\text{train}})$ and $f(\mathbf{u}_{\text{test}})$, and ρ is the correlation coefficient. We set $\mu_{\text{train}} = \mu_{\text{test}} = 0$ to reflect our zero prior knowledge of f over its range. The resulting joint Gaussian distribution is represented by the contours in Fig. 12. To evaluate the shape f at the test point, we fix $f(\mathbf{u}_{\text{train}})$ to its known value, indicated by the square point in Fig. 12. The possible values of $f(\mathbf{u}_{\text{test}})$ are now constrained to lie along the horizontal line, giving rise to the conditional Gaussian distribution indicated by the dashed curve. The mean of the conditional Gaussian is taken to be the value of the shape at the test point.

In this analysis, the conditioning process described above is generalized to $N + 1$ dimensions to accommodate all N training points and one test point at which the shape f is evaluated. The mean, μ_{N+1} , and variance, σ_{N+1}^2 , of f at test point \mathbf{u}_{N+1} are given by:

$$\mu_{N+1} = \mathbf{k}^T \mathbf{C}_N^{-1} \mathbf{t}, \quad (16)$$

$$\sigma_{N+1}^2 = c - \mathbf{k}^T \mathbf{C}_N^{-1} \mathbf{k}, \quad (17)$$

where \mathbf{t} is a column vector containing the $f(\mathbf{u}_i)$ values for all N training points, $\mathbf{k} = \text{cov}(f(\mathbf{u}_i), f(\mathbf{u}_{N+1}))$ is the covariance between the value of f at the i th training point and

the value at the test point, and $c = \text{cov}(f(\mathbf{u}_{N+1}), f(\mathbf{u}_{N+1}))$. The matrix $\mathbf{C}_N = \text{cov}(f(\mathbf{u}_i), f(\mathbf{u}_j))$ is the $N \times N$ covariance matrix expressing the joint Gaussian distribution between the values of f at all N training points. In this analysis, the value of f at each point is given by the mean defined in Eq. (16). The variance in Eq. (17) is provided here for completeness.

The covariance $\text{cov}(f(\mathbf{u}_i), f(\mathbf{u}_j))$ between any two points is determined by a kernel function that is set by the analyzer. The kernel function defines the covariance matrix \mathbf{C}_N in Eqs. (16) and (17), and its properties determine the smoothness characteristics of the final shape. A conventional choice for the GP kernel function is a Gaussian—this ensures that the correlation between any two points is suppressed at a large separation. In practice, the kernel is a three-dimensional function that controls the smoothness of the shape along x , M_t , and JSF. It also includes a correlation term between M_t and JSF to reflect the kinematic relationship between them. The result is a product of a one-dimensional Gaussian (controlling the smoothness along x) with a two-dimensional Gaussian (controlling the smoothness along M_t and JSF). For any two points \mathbf{u}_i and \mathbf{u}_j on the shape, the kernel is given by:

$$\begin{aligned} \text{cov}(f(\mathbf{u}_i), f(\mathbf{u}_j)) = N_1 \left[N_2 \exp \left\{ -\frac{1}{2\theta_1^2} (x_i - x_j)^2 \right\} \right. \\ \left. \exp \left\{ -\frac{1}{2(1-\rho^2)} \left(\frac{1}{\theta_2^2} (M_{ti} - M_{tj})^2 + \frac{1}{\theta_3^2} (\text{JSF}_i - \text{JSF}_j)^2 \right. \right. \right. \\ \left. \left. \left. - \frac{2\rho}{\theta_2\theta_3} (M_{ti} - M_{tj})(\text{JSF}_i - \text{JSF}_j) \right) \right\} + \sigma_i^2 \delta_{ij} \right]. \quad (18) \end{aligned}$$

Here, N_1 , N_2 , θ_1 , θ_2 , θ_3 , and ρ are the GP hyperparameters, σ_i is a noise parameter that accounts for the statistical uncertainty on the distribution bin underlying each training point, and δ_{ij} is the Kronecker delta function. The terms inside the exponentials specify the covariance between any two values of the shape as a function of their corresponding x , M_t , and JSF. The hyperparameters θ_1 , θ_2 , and θ_3 specify the length scales over which the GP shape is allowed to vary, and ρ is a correlation coefficient that couples the M_t and JSF parameters. The hyperparameter N_1 specifies the overall normalization of the kernel function, and N_2 determines the relative normalization between the Gaussian and noise terms.

The values of all hyperparameters are determined with the help of a cross-validation likelihood fit [12], conducted for each observable separately. The length scale hyperparameters (θ_1 , θ_2 , and θ_3) must be small enough for the GP shape to pass through the training points, and large enough for the shape to interpolate smoothly between them. Hyperparameters that are underestimated satisfy the former criterion, but cause overfitting to occur in the resulting GP shape. This creates a noisy interpolation between training points, and may lead to bias in the measured value of M_t and its uncertainties. In this analysis, the GP shapes are checked for overfitting effects using the local shape sensitivity function described in Appendix A.

C The CMS Collaboration

Yerevan Physics Institute, Yerevan, Armenia

A.M. Sirunyan, A. Tumasyan

Institut für Hochenergiephysik, Wien, Austria

W. Adam, E. Asilar, T. Bergauer, J. Brandstetter, E. Brondolin, M. Dragicevic, J. Erö, M. Flechl, M. Friedl, R. Frühwirth¹, V.M. Ghete, C. Hartl, N. Hörmann, J. Hrubec, M. Jeitler¹, A. König, I. Krätschmer, D. Liko, T. Matsushita, I. Mikulec, D. Rabadý, N. Rad, B. Rahbaran, H. Rohringer, J. Schieck¹, J. Strauss, W. Waltenberger, C.-E. Wulz¹

Institute for Nuclear Problems, Minsk, Belarus

O. Dvornikov, V. Makarenko, V. Mossolov, J. Suarez Gonzalez, V. Zykunov

National Centre for Particle and High Energy Physics, Minsk, Belarus

N. Shumeiko

Universiteit Antwerpen, Antwerpen, Belgium

S. Alderweireldt, E.A. De Wolf, X. Janssen, J. Lauwers, M. Van De Klundert, H. Van Haevermaet, P. Van Mechelen, N. Van Remortel, A. Van Spilbeek

Vrije Universiteit Brussel, Brussel, Belgium

S. Abu Zeid, F. Blekman, J. D'Hondt, N. Daci, I. De Bruyn, K. Deroover, S. Lowette, S. Moortgat, L. Moreels, A. Olbrechts, Q. Python, K. Skovpen, S. Tavernier, W. Van Doninck, P. Van Mulders, I. Van Parijs

Université Libre de Bruxelles, Bruxelles, Belgium

H. Brun, B. Clerbaux, G. De Lentdecker, H. Delannoy, G. Fasanella, L. Favart, R. Goldouzian, A. Grebenyuk, G. Karapostoli, T. Lenzi, A. Léonard, J. Luetic, T. Maerschalk, A. Marinov, A. Randle-conde, T. Seva, C. Vander Velde, P. Vanlaer, D. Vannerom, R. Yonamine, F. Zenoni, F. Zhang²

Ghent University, Ghent, Belgium

T. Cornelis, D. Dobur, A. Fagot, M. Gul, I. Khvastunov, D. Poyraz, S. Salva, R. Schöfbeck, M. Tytgat, W. Van Driessche, E. Yazgan, N. Zaganidis

Université Catholique de Louvain, Louvain-la-Neuve, Belgium

H. Bakhshiansohi, O. Bondu, S. Brochet, G. Bruno, A. Caudron, S. De Visscher, C. Delaere, M. Delcourt, B. Francois, A. Giammanco, A. Jafari, M. Komm, G. Krintiras, V. Lemaitre, A. Magitteri, A. Mertens, M. Musich, K. Piotrkowski, L. Quertenmont, M. Selvaggi, M. Vidal Marono, S. Wertz

Université de Mons, Mons, Belgium

N. Bely

Centro Brasileiro de Pesquisas Físicas, Rio de Janeiro, Brazil

W.L. Aldá Júnior, F.L. Alves, G.A. Alves, L. Brito, C. Hensel, A. Moraes, M.E. Pol, P. Rebello Teles

Universidade do Estado do Rio de Janeiro, Rio de Janeiro, Brazil

E. Belchior Batista Das Chagas, W. Carvalho, J. Chinellato³, A. Custódio, E.M. Da Costa, G.G. Da Silveira⁴, D. De Jesus Damiao, C. De Oliveira Martins, S. Fonseca De Souza, L.M. Huertas Guativa, H. Malbouisson, D. Matos Figueiredo, C. Mora Herrera, L. Mundim, H. Nogima, W.L. Prado Da Silva, A. Santoro, A. Sznajder, E.J. Tonelli Manganote³, F. Torres Da Silva De Araujo, A. Vilela Pereira

Universidade Estadual Paulista ^a, Universidade Federal do ABC ^b, São Paulo, Brazil

S. Ahuja^a, C.A. Bernardes^a, S. Dogra^a, T.R. Fernandez Perez Tomei^a, E.M. Gregores^b, P.G. Mercadante^b, C.S. Moon^a, S.F. Novaes^a, Sandra S. Padula^a, D. Romero Abad^b, J.C. Ruiz Vargas^a

Institute for Nuclear Research and Nuclear Energy, Sofia, Bulgaria

A. Aleksandrov, R. Hadjiiska, P. Iaydjiev, M. Rodozov, S. Stoykova, G. Sultanov, M. Vutova

University of Sofia, Sofia, Bulgaria

A. Dimitrov, I. Glushkov, L. Litov, B. Pavlov, P. Petkov

Beihang University, Beijing, China

W. Fang⁵

Institute of High Energy Physics, Beijing, China

M. Ahmad, J.G. Bian, G.M. Chen, H.S. Chen, M. Chen, Y. Chen, T. Cheng, C.H. Jiang, D. Leggat, Z. Liu, F. Romeo, M. Ruan, S.M. Shaheen, A. Spiezia, J. Tao, C. Wang, Z. Wang, H. Zhang, J. Zhao

State Key Laboratory of Nuclear Physics and Technology, Peking University, Beijing, China

Y. Ban, G. Chen, Q. Li, S. Liu, Y. Mao, S.J. Qian, D. Wang, Z. Xu

Universidad de Los Andes, Bogota, Colombia

C. Avila, A. Cabrera, L.F. Chaparro Sierra, C. Florez, J.P. Gomez, C.F. González Hernández, J.D. Ruiz Alvarez⁶, J.C. Sanabria

University of Split, Faculty of Electrical Engineering, Mechanical Engineering and Naval Architecture, Split, Croatia

N. Godinovic, D. Lelas, I. Puljak, P.M. Ribeiro Cipriano, T. Sculac

University of Split, Faculty of Science, Split, Croatia

Z. Antunovic, M. Kovac

Institute Rudjer Boskovic, Zagreb, Croatia

V. Brigljevic, D. Ferencek, K. Kadija, B. Mesic, T. Susa

University of Cyprus, Nicosia, Cyprus

M.W. Ather, A. Attikis, G. Mavromanolakis, J. Mousa, C. Nicolaou, F. Ptochos, P.A. Razis, H. Rykaczewski

Charles University, Prague, Czech Republic

M. Finger⁷, M. Finger Jr.⁷

Universidad San Francisco de Quito, Quito, Ecuador

E. Carrera Jarrin

Academy of Scientific Research and Technology of the Arab Republic of Egypt, Egyptian Network of High Energy Physics, Cairo, Egypt

Y. Assran^{8,9}, T. Elkafrawy¹⁰, A. Mahrous¹¹

National Institute of Chemical Physics and Biophysics, Tallinn, Estonia

M. Kadastik, L. Perrini, M. Raidal, A. Tiko, C. Veelken

Department of Physics, University of Helsinki, Helsinki, Finland

P. Eerola, J. Pekkanen, M. Voutilainen

Helsinki Institute of Physics, Helsinki, Finland

J. Härkönen, T. Järvinen, V. Karimäki, R. Kinnunen, T. Lampén, K. Lassila-Perini, S. Lehti, T. Lindén, P. Luukka, J. Tuominiemi, E. Tuovinen, L. Wendland

Lappeenranta University of Technology, Lappeenranta, Finland

J. Talvitie, T. Tuuva

IRFU, CEA, Université Paris-Saclay, Gif-sur-Yvette, France

M. Besancon, F. Couderc, M. Dejardin, D. Denegri, B. Fabbro, J.L. Faure, C. Favaro, F. Ferri, S. Ganjour, S. Ghosh, A. Givernaud, P. Gras, G. Hamel de Monchenault, P. Jarry, I. Kucher, E. Locci, M. Machet, J. Malcles, J. Rander, A. Rosowsky, M. Titov

Laboratoire Leprince-Ringuet, Ecole polytechnique, CNRS/IN2P3, Université Paris-Saclay

A. Abdulsalam, I. Antropov, S. Baffioni, F. Beaudette, P. Busson, L. Cadamuro, E. Chapon, C. Charlot, O. Davignon, R. Granier de Cassagnac, M. Jo, S. Lisniak, P. Miné, M. Nguyen, C. Ochando, G. Ortona, P. Paganini, P. Pigard, S. Regnard, R. Salerno, Y. Sirois, A.G. Stahl Leitner, T. Strebler, Y. Yilmaz, A. Zabi, A. Zghiche

Université de Strasbourg, CNRS, IPHC UMR 7178, F-67000 Strasbourg, France

J.-L. Agram¹², J. Andrea, D. Bloch, J.-M. Brom, M. Buttignol, E.C. Chabert, N. Chanon, C. Collard, E. Conte¹², X. Coubez, J.-C. Fontaine¹², D. Gelé, U. Goerlach, A.-C. Le Bihan, P. Van Hove

Centre de Calcul de l'Institut National de Physique Nucleaire et de Physique des Particules, CNRS/IN2P3, Villeurbanne, France

S. Gadrat

Université de Lyon, Université Claude Bernard Lyon 1, CNRS-IN2P3, Institut de Physique Nucléaire de Lyon, Villeurbanne, France

S. Beauceron, C. Bernet, G. Boudoul, C.A. Carrillo Montoya, R. Chierici, D. Contardo, B. Courbon, P. Depasse, H. El Mamouni, J. Fay, L. Finco, S. Gascon, M. Gouzevitch, G. Grenier, B. Ille, F. Lagarde, I.B. Laktineh, M. Lethuillier, L. Mirabito, A.L. Pequegnot, S. Perries, A. Popov¹³, V. Sordini, M. Vander Donckt, P. Verdier, S. Viret

Georgian Technical University, Tbilisi, Georgia

A. Khvedelidze⁷

Tbilisi State University, Tbilisi, Georgia

Z. Tsamalaidze⁷

RWTH Aachen University, I. Physikalisches Institut, Aachen, Germany

C. Autermann, S. Beranek, L. Feld, M.K. Kiesel, K. Klein, M. Lipinski, M. Preuten, C. Schomakers, J. Schulz, T. Verlage

RWTH Aachen University, III. Physikalisches Institut A, Aachen, Germany

A. Albert, M. Brodski, E. Dietz-Laursonn, D. Duchardt, M. Endres, M. Erdmann, S. Erdweg, T. Esch, R. Fischer, A. Güth, M. Hamer, T. Hebbeker, C. Heidemann, K. Hoepfner, S. Knutzen, M. Merschmeyer, A. Meyer, P. Millet, S. Mukherjee, M. Olschewski, K. Padeken, T. Pook, M. Radziej, H. Reithler, M. Rieger, F. Scheuch, L. Sonnenschein, D. Teyssier, S. Thüer

RWTH Aachen University, III. Physikalisches Institut B, Aachen, Germany

V. Cherepanov, G. Flügge, B. Kargoll, T. Kress, A. Künsken, J. Lingemann, T. Müller, A. Nehr Korn, A. Nowack, C. Pistone, O. Pooth, A. Stahl¹⁴

Deutsches Elektronen-Synchrotron, Hamburg, Germany

M. Aldaya Martin, T. Arndt, C. Asawatangtrakuldee, K. Beernaert, O. Behnke, U. Behrens, A.A. Bin Anuar, K. Borras¹⁵, A. Campbell, P. Connor, C. Contreras-Campana, F. Costanza, C. Diez Pardos, G. Dolinska, G. Eckerlin, D. Eckstein, T. Eichhorn, E. Eren, E. Gallo¹⁶, J. Garay Garcia, A. Geiser, A. Gizhko, J.M. Grados Luyando, A. Grohsjean, P. Gunnellini, A. Harb, J. Hauk, M. Hempel¹⁷, H. Jung, A. Kalogeropoulos, O. Karacheban¹⁷, M. Kasemann, J. Keaveney, C. Kleinwort, I. Korol, D. Krücker, W. Lange, A. Lelek, T. Lenz, J. Leonard, K. Lipka, A. Lobanov, W. Lohmann¹⁷, R. Mankel, I.-A. Melzer-Pellmann, A.B. Meyer, G. Mittag, J. Mnich, A. Mussgiller, D. Pitzl, R. Placakyte, A. Raspereza, B. Roland, M.Ö. Sahin, P. Saxena, T. Schoerner-Sadenius, S. Spannagel, N. Stefaniuk, G.P. Van Onsem, R. Walsh, C. Wissing

University of Hamburg, Hamburg, Germany

V. Blobel, M. Centis Vignali, A.R. Draeger, T. Dreyer, E. Garutti, D. Gonzalez, J. Haller, M. Hoffmann, A. Junkes, R. Klanner, R. Kogler, N. Kovalchuk, S. Kurz, T. Lapsien, I. Marchesini, D. Marconi, M. Meyer, M. Niedziela, D. Nowatschin, F. Pantaleo¹⁴, T. Peiffer, A. Perieanu, C. Scharf, P. Schleper, A. Schmidt, S. Schumann, J. Schwandt, J. Sonneveld, H. Stadie, G. Steinbrück, F.M. Stober, M. Stöver, H. Tholen, D. Troendle, E. Usai, L. Vanelderen, A. Vanhoefer, B. Vormwald

Institut für Experimentelle Kernphysik, Karlsruhe, Germany

M. Akbiyik, C. Barth, S. Baur, C. Baus, J. Berger, E. Butz, R. Caspart, T. Chwalek, F. Colombo, W. De Boer, A. Dierlamm, S. Fink, B. Freund, R. Friese, M. Giffels, A. Gilbert, P. Goldenzweig, D. Haitz, F. Hartmann¹⁴, S.M. Heindl, U. Husemann, F. Kassel¹⁴, I. Katkov¹³, S. Kudella, H. Mildner, M.U. Mozer, Th. Müller, M. Plagge, G. Quast, K. Rabbertz, S. Röcker, F. Roscher, M. Schröder, I. Shvetsov, G. Sieber, H.J. Simonis, R. Ulrich, S. Wayand, M. Weber, T. Weiler, S. Williamson, C. Wöhrmann, R. Wolf

Institute of Nuclear and Particle Physics (INPP), NCSR Demokritos, Aghia Paraskevi, Greece

G. Anagnostou, G. Daskalakis, T. Gerasis, V.A. Giakoumopoulou, A. Kyriakis, D. Loukas, I. Topsis-Giotis

National and Kapodistrian University of Athens, Athens, Greece

S. Kesisoglou, A. Panagiotou, N. Saoulidou, E. Tziaferi

National Technical University of Athens, Athens, Greece

K. Kousouris

University of Ioánnina, Ioánnina, Greece

I. Evangelou, G. Flouris, C. Foudas, P. Kokkas, N. Loukas, N. Manthos, I. Papadopoulos, E. Paradas

MTA-ELTE Lendület CMS Particle and Nuclear Physics Group, Eötvös Loránd University, Budapest, Hungary

N. Filipovic, G. Pasztor

Wigner Research Centre for Physics, Budapest, Hungary

G. Bencze, C. Hajdu, D. Horvath¹⁸, F. Sikler, V. Veszpremi, G. Vesztergombi¹⁹, A.J. Zsigmond

Institute of Nuclear Research ATOMKI, Debrecen, Hungary

N. Beni, S. Czellar, J. Karancsi²⁰, A. Makovec, J. Molnar, Z. Szillasi

Institute of Physics, University of Debrecen

M. Bartók¹⁹, P. Raics, Z.L. Trocsanyi, B. Ujvari

Indian Institute of Science (IISc)

S. Choudhury, J.R. Komaragiri

National Institute of Science Education and Research, Bhubaneswar, India

S. Bahinipati²¹, S. Bhowmik²², P. Mal, K. Mandal, A. Nayak²³, D.K. Sahoo²¹, N. Sahoo, S.K. Swain

Panjab University, Chandigarh, India

S. Bansal, S.B. Beri, V. Bhatnagar, R. Chawla, U. Bhawandeep, A.K. Kalsi, A. Kaur, M. Kaur, R. Kumar, P. Kumari, A. Mehta, M. Mittal, J.B. Singh, G. Walia

University of Delhi, Delhi, India

Ashok Kumar, A. Bhardwaj, B.C. Choudhary, R.B. Garg, S. Keshri, A. Kumar, S. Malhotra, M. Naimuddin, K. Ranjan, R. Sharma, V. Sharma

Saha Institute of Nuclear Physics, Kolkata, India

R. Bhattacharya, S. Bhattacharya, K. Chatterjee, S. Dey, S. Dutt, S. Dutta, S. Ghosh, N. Majumdar, A. Modak, K. Mondal, S. Mukhopadhyay, S. Nandan, A. Purohit, A. Roy, D. Roy, S. Roy Chowdhury, S. Sarkar, M. Sharan, S. Thakur

Indian Institute of Technology Madras, Madras, India

P.K. Behera

Bhabha Atomic Research Centre, Mumbai, India

R. Chudasama, D. Dutta, V. Jha, V. Kumar, A.K. Mohanty¹⁴, P.K. Netrakanti, L.M. Pant, P. Shukla, A. Topkar

Tata Institute of Fundamental Research-A, Mumbai, India

T. Aziz, S. Dugad, G. Kole, B. Mahakud, S. Mitra, G.B. Mohanty, B. Parida, N. Sur, B. Sutar

Tata Institute of Fundamental Research-B, Mumbai, India

S. Banerjee, R.K. Dewanjee, S. Ganguly, M. Guchait, Sa. Jain, S. Kumar, M. Maity²², G. Majumder, K. Mazumdar, T. Sarkar²², N. Wickramage²⁴

Indian Institute of Science Education and Research (IISER), Pune, India

S. Chauhan, S. Dube, V. Hegde, A. Kapoor, K. Kothekar, S. Pandey, A. Rane, S. Sharma

Institute for Research in Fundamental Sciences (IPM), Tehran, Iran

S. Chenarani²⁵, E. Eskandari Tadavani, S.M. Etesami²⁵, M. Khakzad, M. Mohammadi Najafabadi, M. Naseri, S. Paktinat Mehdiabadi²⁶, F. Rezaei Hosseinabadi, B. Safarzadeh²⁷, M. Zeinali

University College Dublin, Dublin, Ireland

M. Felcini, M. Grunewald

INFN Sezione di Bari ^a, Università di Bari ^b, Politecnico di Bari ^c, Bari, Italy

M. Abbrescia^{a,b}, C. Calabria^{a,b}, C. Caputo^{a,b}, A. Colaleo^a, D. Creanza^{a,c}, L. Cristella^{a,b}, N. De Filippis^{a,c}, M. De Palma^{a,b}, L. Fiore^a, G. Iaselli^{a,c}, G. Maggi^{a,c}, M. Maggi^a, G. Miniello^{a,b}, S. My^{a,b}, S. Nuzzo^{a,b}, A. Pompili^{a,b}, G. Pugliese^{a,c}, R. Radogna^{a,b}, A. Ranieri^a, G. Selvaggi^{a,b}, A. Sharma^a, L. Silvestris^{a,14}, R. Venditti^{a,b}, P. Verwilligen^a

INFN Sezione di Bologna ^a, Università di Bologna ^b, Bologna, Italy

G. Abbiendi^a, C. Battilana, D. Bonacorsi^{a,b}, S. Braibant-Giacomelli^{a,b}, L. Brigliadori^{a,b}, R. Campanini^{a,b}, P. Capiluppi^{a,b}, A. Castro^{a,b}, F.R. Cavallo^a, S.S. Chhibra^{a,b}, G. Codispoti^{a,b}, M. Cuffiani^{a,b}, G.M. Dallavalle^a, F. Fabbri^a, A. Fanfani^{a,b}, D. Fasanella^{a,b}, P. Giacomelli^a,

C. Grandi^a, L. Guiducci^{a,b}, S. Marcellini^a, G. Masetti^a, A. Montanari^a, F.L. Navarria^{a,b}, A. Perrotta^a, A.M. Rossi^{a,b}, T. Rovelli^{a,b}, G.P. Siroli^{a,b}, N. Tosi^{a,b,14}

INFN Sezione di Catania^a, Università di Catania^b, Catania, Italy

S. Albergo^{a,b}, S. Costa^{a,b}, A. Di Mattia^a, F. Giordano^{a,b}, R. Potenza^{a,b}, A. Tricomi^{a,b}, C. Tuve^{a,b}

INFN Sezione di Firenze^a, Università di Firenze^b, Firenze, Italy

G. Barbagli^a, V. Ciulli^{a,b}, C. Civinini^a, R. D'Alessandro^{a,b}, E. Focardi^{a,b}, P. Lenzi^{a,b}, M. Meschini^a, S. Paoletti^a, L. Russo^{a,28}, G. Sguazzoni^a, D. Strom^a, L. Viliani^{a,b,14}

INFN Laboratori Nazionali di Frascati, Frascati, Italy

L. Benussi, S. Bianco, F. Fabbri, D. Piccolo, F. Primavera¹⁴

INFN Sezione di Genova^a, Università di Genova^b, Genova, Italy

V. Calvelli^{a,b}, F. Ferro^a, M.R. Monge^{a,b}, E. Robutti^a, S. Tosi^{a,b}

INFN Sezione di Milano-Bicocca^a, Università di Milano-Bicocca^b, Milano, Italy

L. Brianza^{a,b,14}, F. Brivio^{a,b}, V. Ciriolo, M.E. Dinardo^{a,b}, S. Fiorendi^{a,b,14}, S. Gennai^a, A. Ghezzi^{a,b}, P. Govoni^{a,b}, M. Malberti^{a,b}, S. Malvezzi^a, R.A. Manzoni^{a,b}, D. Menasce^a, L. Moroni^a, M. Paganoni^{a,b}, D. Pedrini^a, S. Pigazzini^{a,b}, S. Ragazzi^{a,b}, T. Tabarelli de Fatis^{a,b}

INFN Sezione di Napoli^a, Università di Napoli 'Federico II'^b, Napoli, Italy, Università della Basilicata^c, Potenza, Italy, Università G. Marconi^d, Roma, Italy

S. Buontempo^a, N. Cavallo^{a,c}, G. De Nardo, S. Di Guida^{a,d,14}, M. Esposito^{a,b}, F. Fabozzi^{a,c}, F. Fienga^{a,b}, A.O.M. Iorio^{a,b}, G. Lanza^a, L. Lista^a, S. Meola^{a,d,14}, P. Paolucci^{a,14}, C. Sciacca^{a,b}, E. Thyssen^a

INFN Sezione di Padova^a, Università di Padova^b, Padova, Italy, Università di Trento^c, Trento, Italy

P. Azzi^{a,14}, N. Bacchetta^a, L. Benato^{a,b}, D. Bisello^{a,b}, A. Boletti^{a,b}, R. Carlin^{a,b}, P. Checchia^a, M. Dall'Osso^{a,b}, P. De Castro Manzano^a, T. Dorigo^a, U. Dosselli^a, F. Gasparini^{a,b}, U. Gasparini^{a,b}, S. Lacaprara^a, M. Margoni^{a,b}, A.T. Meneguzzo^{a,b}, J. Pazzini^{a,b}, N. Pozzobon^{a,b}, P. Ronchese^{a,b}, R. Rossin^{a,b}, F. Simonetto^{a,b}, E. Torassa^a, S. Ventura^a, M. Zanetti^{a,b}, P. Zotto^{a,b}, G. Zumerle^{a,b}

INFN Sezione di Pavia^a, Università di Pavia^b, Pavia, Italy

A. Braghieri^a, F. Fallavollita^{a,b}, A. Magnani^{a,b}, P. Montagna^{a,b}, S.P. Ratti^{a,b}, V. Re^a, M. Ressegotti, C. Riccardi^{a,b}, P. Salvini^a, I. Vai^{a,b}, P. Vitulo^{a,b}

INFN Sezione di Perugia^a, Università di Perugia^b, Perugia, Italy

L. Alunni Solestizi^{a,b}, G.M. Bilei^a, D. Ciangottini^{a,b}, L. Fanò^{a,b}, P. Lariccia^{a,b}, R. Leonardi^{a,b}, G. Mantovani^{a,b}, V. Mariani^{a,b}, M. Menichelli^a, A. Saha^a, A. Santocchia^{a,b}

INFN Sezione di Pisa^a, Università di Pisa^b, Scuola Normale Superiore di Pisa^c, Pisa, Italy

K. Androsov^{a,28}, P. Azzurri^{a,14}, G. Bagliesi^a, J. Bernardini^a, T. Boccali^a, R. Castaldi^a, M.A. Ciocci^{a,b,28}, R. Dell'Orso^a, G. Fedi^a, A. Giassi^a, M.T. Grippo^{a,28}, F. Ligabue^{a,c}, T. Lomtadze^a, L. Martini^{a,b}, A. Messineo^{a,b}, F. Palla^a, A. Rizzi^{a,b}, A. Savoy-Navarro^{a,29}, P. Spagnolo^a, R. Tenchini^a, G. Tonelli^{a,b}, A. Venturi^a, P.G. Verdini^a

INFN Sezione di Roma^a, Sapienza Università di Roma^b

L. Barone, F. Cavallari, M. Cipriani, D. Del Re¹⁴, M. Diemoz, S. Gelli, E. Longo, F. Margaroli, B. Marzocchi, P. Meridiani, G. Organtini, R. Paramatti, F. Preiato, S. Rahatlou, C. Rovelli, F. Santanastasio

INFN Sezione di Torino ^a, Università di Torino ^b, Torino, Italy, Università del Piemonte Orientale ^c, Novara, Italy

N. Amapane^{a,b}, R. Arcidiacono^{a,c,14}, S. Argiro^{a,b}, M. Arneodo^{a,c}, N. Bartosik^a, R. Bellan^{a,b}, C. Biino^a, N. Cartiglia^a, F. Cenna^{a,b}, M. Costa^{a,b}, R. Covarelli^{a,b}, A. Degano^{a,b}, N. Demaria^a, B. Kiani^{a,b}, C. Mariotti^a, S. Maselli^a, E. Migliore^{a,b}, V. Monaco^{a,b}, E. Monteil^{a,b}, M. Monteno^a, M.M. Obertino^{a,b}, L. Pacher^{a,b}, N. Pastrone^a, M. Pelliccioni^a, G.L. Pinna Angioni^{a,b}, F. Ravera^{a,b}, A. Romero^{a,b}, M. Ruspa^{a,c}, R. Sacchi^{a,b}, K. Shchelina^{a,b}, V. Sola^a, A. Solano^{a,b}, A. Staiano^a, P. Traczyk^{a,b}

INFN Sezione di Trieste ^a, Università di Trieste ^b, Trieste, Italy

S. Belforte^a, M. Casarsa^a, F. Cossutti^a, G. Della Ricca^{a,b}, A. Zanetti^a

Kyungpook National University, Daegu, Korea

D.H. Kim, G.N. Kim, M.S. Kim, J. Lee, S. Lee, S.W. Lee, Y.D. Oh, S. Sekmen, D.C. Son, Y.C. Yang

Chonbuk National University, Jeonju, Korea

A. Lee

Chonnam National University, Institute for Universe and Elementary Particles, Kwangju, Korea

H. Kim

Hanyang University, Seoul, Korea

J.A. Brochero Cifuentes, T.J. Kim

Korea University, Seoul, Korea

S. Cho, S. Choi, Y. Go, D. Gyun, S. Ha, B. Hong, Y. Jo, Y. Kim, K. Lee, K.S. Lee, S. Lee, J. Lim, S.K. Park, Y. Roh

Seoul National University, Seoul, Korea

J. Almond, J. Kim, H. Lee, S.B. Oh, B.C. Radburn-Smith, S.h. Seo, U.K. Yang, H.D. Yoo, G.B. Yu

University of Seoul, Seoul, Korea

M. Choi, H. Kim, J.H. Kim, J.S.H. Lee, I.C. Park, G. Ryu, M.S. Ryu

Sungkyunkwan University, Suwon, Korea

Y. Choi, J. Goh, C. Hwang, J. Lee, I. Yu

Vilnius University, Vilnius, Lithuania

V. Dudenas, A. Juodagalvis, J. Vaitkus

National Centre for Particle Physics, Universiti Malaya, Kuala Lumpur, Malaysia

I. Ahmed, Z.A. Ibrahim, M.A.B. Md Ali³⁰, F. Mohamad Idris³¹, W.A.T. Wan Abdullah, M.N. Yusli, Z. Zolkapli

Centro de Investigacion y de Estudios Avanzados del IPN, Mexico City, Mexico

H. Castilla-Valdez, E. De La Cruz-Burelo, I. Heredia-De La Cruz³², A. Hernandez-Almada, R. Lopez-Fernandez, R. Magaña Villalba, J. Mejia Guisao, A. Sanchez-Hernandez

Universidad Iberoamericana, Mexico City, Mexico

S. Carrillo Moreno, C. Oropeza Barrera, F. Vazquez Valencia

Benemerita Universidad Autonoma de Puebla, Puebla, Mexico

S. Carpinteyro, I. Pedraza, H.A. Salazar Ibarguen, C. Uribe Estrada

Universidad Autónoma de San Luis Potosí, San Luis Potosí, Mexico

A. Morelos Pineda

University of Auckland, Auckland, New Zealand

D. Krofcheck

University of Canterbury, Christchurch, New Zealand

P.H. Butler

National Centre for Physics, Quaid-I-Azam University, Islamabad, Pakistan

A. Ahmad, M. Ahmad, Q. Hassan, H.R. Hoorani, W.A. Khan, A. Saddique, M.A. Shah, M. Shoaib, M. Waqas

National Centre for Nuclear Research, Swierk, Poland

H. Bialkowska, M. Bluj, B. Boimska, T. Frueboes, M. Górski, M. Kazana, K. Nawrocki, K. Romanowska-Rybinska, M. Szleper, P. Zalewski

Institute of Experimental Physics, Faculty of Physics, University of Warsaw, Warsaw, Poland

K. Bunkowski, A. Byszuk³³, K. Doroba, A. Kalinowski, M. Konecki, J. Krolikowski, M. Misiura, M. Olszewski, A. Pyskir, M. Walczak

Laboratório de Instrumentação e Física Experimental de Partículas, Lisboa, Portugal

P. Bargassa, C. Beirão Da Cruz E Silva, B. Calpas, A. Di Francesco, P. Faccioli, M. Gallinaro, J. Hollar, N. Leonardo, L. Lloret Iglesias, M.V. Nemallapudi, J. Seixas, O. Toldaiev, D. Vadrucchio, J. Varela

Joint Institute for Nuclear Research, Dubna, Russia

S. Afanasiev, P. Bunin, M. Gavrilenko, I. Golutvin, I. Gorbunov, A. Kamenev, V. Karjavin, A. Lanev, A. Malakhov, V. Matveev^{34,35}, V. Palichik, V. Perelygin, S. Shmatov, S. Shulha, N. Skatchkov, V. Smirnov, N. Voytishin, A. Zarubin

Petersburg Nuclear Physics Institute, Gatchina (St. Petersburg), Russia

L. Chtchipunov, V. Golovtsov, Y. Ivanov, V. Kim³⁶, E. Kuznetsova³⁷, V. Murzin, V. Oreshkin, V. Sulimov, A. Vorobyev

Institute for Nuclear Research, Moscow, Russia

Yu. Andreev, A. Dermenev, S. Gninenko, N. Golubev, A. Karneyeu, M. Kirsanov, N. Krasnikov, A. Pashenkov, D. Tlisov, A. Toropin

Institute for Theoretical and Experimental Physics, Moscow, Russia

V. Epshteyn, V. Gavrilov, N. Lychkovskaya, V. Popov, I. Pozdnyakov, G. Safronov, A. Spiridonov, M. Toms, E. Vlasov, A. Zhokin

Moscow Institute of Physics and Technology, Moscow, Russia

T. Aushev, A. Bylinkin³⁵

National Research Nuclear University 'Moscow Engineering Physics Institute' (MEPhI), Moscow, Russia

M. Chadeeva³⁸, O. Markin, E. Tarkovskii

P.N. Lebedev Physical Institute, Moscow, Russia

V. Andreev, M. Azarkin³⁵, I. Dremin³⁵, M. Kirakosyan, A. Leonidov³⁵, A. Terkulov

Skobeltsyn Institute of Nuclear Physics, Lomonosov Moscow State University, Moscow, Russia

A. Baskakov, A. Belyaev, E. Boos, V. Bunichev, M. Dubinin³⁹, L. Dudko, V. Klyukhin, O. Kodolova, N. Korneeva, I. Lokhtin, I. Miagkov, S. Obraztsov, M. Perfilov, V. Savrin, P. Volkov

Novosibirsk State University (NSU), Novosibirsk, RussiaV. Blinov⁴⁰, Y.Skovpen⁴⁰, D. Shtol⁴⁰**State Research Center of Russian Federation, Institute for High Energy Physics, Protvino, Russia**

I. Azhgirey, I. Bayshev, S. Bitioukov, D. Elumakhov, V. Kachanov, A. Kalinin, D. Konstantinov, V. Krychkine, V. Petrov, R. Ryutin, A. Sobol, S. Troshin, N. Tyurin, A. Uzunian, A. Volkov

University of Belgrade, Faculty of Physics and Vinca Institute of Nuclear Sciences, Belgrade, SerbiaP. Adzic⁴¹, P. Cirkovic, D. Devetak, M. Dordevic, J. Milosevic, V. Rekovic**Centro de Investigaciones Energéticas Medioambientales y Tecnológicas (CIEMAT), Madrid, Spain**

J. Alcaraz Maestre, M. Barrio Luna, E. Calvo, M. Cerrada, M. Chamizo Llatas, N. Colino, B. De La Cruz, A. Delgado Peris, A. Escalante Del Valle, C. Fernandez Bedoya, J.P. Fernández Ramos, J. Flix, M.C. Fouz, P. Garcia-Abia, O. Gonzalez Lopez, S. Goy Lopez, J.M. Hernandez, M.I. Josa, E. Navarro De Martino, A. Pérez-Calero Yzquierdo, J. Puerta Pelayo, A. Quintario Olmeda, I. Redondo, L. Romero, M.S. Soares

Universidad Autónoma de Madrid, Madrid, Spain

J.F. de Trocóniz, M. Missiroli, D. Moran

Universidad de Oviedo, Oviedo, Spain

J. Cuevas, C. Erice, J. Fernandez Menendez, I. Gonzalez Caballero, J.R. González Fernández, E. Palencia Cortezon, S. Sanchez Cruz, I. Suárez Andrés, P. Vischia, J.M. Vizan Garcia

Instituto de Física de Cantabria (IFCA), CSIC-Universidad de Cantabria, Santander, Spain

I.J. Cabrillo, A. Calderon, E. Curras, M. Fernandez, J. Garcia-Ferrero, G. Gomez, A. Lopez Virto, J. Marco, C. Martinez Rivero, F. Matorras, J. Piedra Gomez, T. Rodrigo, A. Ruiz-Jimeno, L. Scodellaro, N. Trevisani, I. Vila, R. Vilar Cortabitarte

CERN, European Organization for Nuclear Research, Geneva, SwitzerlandD. Abbaneo, E. Auffray, G. Auzinger, P. Baillon, A.H. Ball, D. Barney, P. Bloch, A. Bocci, C. Botta, T. Camporesi, R. Castello, M. Cepeda, G. Cerminara, Y. Chen, A. Cimmino, D. d'Enterria, A. Dabrowski, V. Daponte, A. David, M. De Gruttola, A. De Roeck, E. Di Marco⁴², M. Dobson, B. Dorney, T. du Pree, D. Duggan, M. Dünser, N. Dupont, A. Elliott-Peisert, P. Everaerts, S. Fartoukh, G. Franzoni, J. Fulcher, W. Funk, D. Gigi, K. Gill, M. Girone, F. Glege, D. Gulhan, S. Gundacker, M. Guthoff, P. Harris, J. Hegeman, V. Innocente, P. Janot, J. Kieseler, H. Kirschenmann, V. Knünz, A. Kornmayer¹⁴, M.J. Kortelainen, M. Krammer¹, C. Lange, P. Lecoq, C. Lourenço, M.T. Lucchini, L. Malgeri, M. Mannelli, A. Martelli, F. Meijers, J.A. Merlin, S. Mersi, E. Meschi, P. Milenovic⁴³, F. Moortgat, S. Morovic, M. Mulders, H. Neugebauer, S. Orfanelli, L. Orsini, L. Pape, E. Perez, M. Peruzzi, A. Petrilli, G. Petrucciani, A. Pfeiffer, M. Pierini, A. Racz, T. Reis, G. Rolandi⁴⁴, M. Rovere, H. Sakulin, J.B. Sauvan, C. Schäfer, C. Schwick, M. Seidel, A. Sharma, P. Silva, P. Sphicas⁴⁵, J. Steggemann, M. Stoye, Y. Takahashi, M. Tosi, D. Treille, A. Triossi, A. Tsiros, V. Veckalns⁴⁶, G.I. Veres¹⁹, M. Verweij, N. Wardle, H.K. Wöhri, A. Zagozdinska³³, W.D. Zeuner**Paul Scherrer Institut, Villigen, Switzerland**

W. Bertl, K. Deiters, W. Erdmann, R. Horisberger, Q. Ingram, H.C. Kaestli, D. Kotlinski, U. Langenegger, T. Rohe, S.A. Wiederkehr

Institute for Particle Physics, ETH Zurich, Zurich, Switzerland

F. Bachmair, L. Bäni, L. Bianchini, B. Casal, G. Dissertori, M. Dittmar, M. Donegà, C. Grab,

C. Heidegger, D. Hits, J. Hoss, G. Kasieczka, W. Lustermann, B. Mangano, M. Marionneau, P. Martinez Ruiz del Arbol, M. Masciovecchio, M.T. Meinhard, D. Meister, F. Micheli, P. Musella, F. Nessi-Tedaldi, F. Pandolfi, J. Pata, F. Pauss, G. Perrin, L. Perrozzi, M. Quitnat, M. Rossini, M. Schönerberger, A. Starodumov⁴⁷, V.R. Tavolaro, K. Theofilatos, R. Wallny

Universität Zürich, Zurich, Switzerland

T.K. Aarrestad, C. Amsler⁴⁸, L. Caminada, M.F. Canelli, A. De Cosa, S. Donato, C. Galloni, A. Hinzmann, T. Hreus, B. Kilminster, J. Ngadiuba, D. Pinna, G. Rauco, P. Robmann, D. Salerno, C. Seitz, Y. Yang, A. Zucchetta

National Central University, Chung-Li, Taiwan

V. Candelise, T.H. Doan, Sh. Jain, R. Khurana, M. Konyushikhin, C.M. Kuo, W. Lin, A. Pozdnyakov, S.S. Yu

National Taiwan University (NTU), Taipei, Taiwan

Arun Kumar, P. Chang, Y.H. Chang, Y. Chao, K.F. Chen, P.H. Chen, F. Fiori, W.-S. Hou, Y. Hsiung, Y.F. Liu, R.-S. Lu, M. Miñano Moya, E. Paganis, A. Psallidas, J.f. Tsai

Chulalongkorn University, Faculty of Science, Department of Physics, Bangkok, Thailand

B. Asavapibhop, G. Singh, N. Srimanobhas, N. Suwonjandee

Cukurova University - Physics Department, Science and Art Faculty

A. Adiguzel, M.N. Bakirci⁴⁹, F. Boran, S. Cerci⁵⁰, S. Damarseckin, Z.S. Demiroglu, C. Dozen, I. Dumanoglu, S. Girgis, G. Gokbulut, Y. Guler, I. Hos⁵¹, E.E. Kangal⁵², O. Kara, A. Kayis Topaksu, U. Kiminsu, M. Oglakci, G. Onengut⁵³, K. Ozdemir⁵⁴, B. Tali⁵⁰, S. Turkcapar, I.S. Zorbakir, C. Zorbilmez

Middle East Technical University, Physics Department, Ankara, Turkey

B. Bilin, S. Bilmis, B. Isildak⁵⁵, G. Karapinar⁵⁶, M. Yalvac, M. Zeyrek

Bogazici University, Istanbul, Turkey

E. Gülmez, M. Kaya⁵⁷, O. Kaya⁵⁸, E.A. Yetkin⁵⁹, T. Yetkin⁶⁰

Istanbul Technical University, Istanbul, Turkey

A. Cakir, K. Cankocak, S. Sen⁶¹

Institute for Scintillation Materials of National Academy of Science of Ukraine, Kharkov, Ukraine

B. Grynyov

National Scientific Center, Kharkov Institute of Physics and Technology, Kharkov, Ukraine

L. Levchuk, P. Sorokin

University of Bristol, Bristol, United Kingdom

R. Aggleton, F. Ball, L. Beck, J.J. Brooke, D. Burns, E. Clement, D. Cussans, H. Flacher, J. Goldstein, M. Grimes, G.P. Heath, H.F. Heath, J. Jacob, L. Kreczko, C. Lucas, D.M. Newbold⁶², S. Paramesvaran, A. Poll, T. Sakuma, S. Seif El Nasr-storey, D. Smith, V.J. Smith

Rutherford Appleton Laboratory, Didcot, United Kingdom

K.W. Bell, A. Belyaev⁶³, C. Brew, R.M. Brown, L. Calligaris, D. Cieri, D.J.A. Cockerill, J.A. Coughlan, K. Harder, S. Harper, E. Olaiya, D. Petyt, C.H. Shepherd-Themistocleous, A. Thea, I.R. Tomalin, T. Williams

Imperial College, London, United Kingdom

M. Baber, R. Bainbridge, O. Buchmuller, A. Bundock, S. Casasso, M. Citron, D. Colling, L. Corpe, P. Dauncey, G. Davies, A. De Wit, M. Della Negra, R. Di Maria, P. Dunne,

A. Elwood, D. Futyan, Y. Haddad, G. Hall, G. Iles, T. James, R. Lane, C. Laner, L. Lyons, A.-M. Magnan, S. Malik, L. Mastrolorenzo, J. Nash, A. Nikitenko⁴⁷, J. Pela, B. Penning, M. Pesaresi, D.M. Raymond, A. Richards, A. Rose, E. Scott, C. Seez, S. Summers, A. Tapper, K. Uchida, M. Vazquez Acosta⁶⁴, T. Virdee¹⁴, J. Wright, S.C. Zenz

Brunel University, Uxbridge, United Kingdom

J.E. Cole, P.R. Hobson, A. Khan, P. Kyberd, I.D. Reid, P. Symonds, L. Teodorescu, M. Turner

Baylor University, Waco, USA

A. Borzou, K. Call, J. Dittmann, K. Hatakeyama, H. Liu, N. Pastika

Catholic University of America

R. Bartek, A. Dominguez

The University of Alabama, Tuscaloosa, USA

A. Buccilli, S.I. Cooper, C. Henderson, P. Rumerio, C. West

Boston University, Boston, USA

D. Arcaro, A. Avetisyan, T. Bose, D. Gastler, D. Rankin, C. Richardson, J. Rohlf, L. Sulak, D. Zou

Brown University, Providence, USA

G. Benelli, D. Cutts, A. Garabedian, J. Hakala, U. Heintz, J.M. Hogan, O. Jesus, K.H.M. Kwok, E. Laird, G. Landsberg, Z. Mao, M. Narain, S. Piperov, S. Sagir, E. Spencer, R. Syarif

University of California, Davis, Davis, USA

R. Breedon, D. Burns, M. Calderon De La Barca Sanchez, S. Chauhan, M. Chertok, J. Conway, R. Conway, P.T. Cox, R. Erbacher, C. Flores, G. Funk, M. Gardner, W. Ko, R. Lander, C. Mclean, M. Mulhearn, D. Pellett, J. Pilot, S. Shalhout, M. Shi, J. Smith, M. Squires, D. Stolp, K. Tos, M. Tripathi

University of California, Los Angeles, USA

M. Bachtis, C. Bravo, R. Cousins, A. Dasgupta, A. Florent, J. Hauser, M. Ignatenko, N. Mccoll, D. Saltzberg, C. Schnaible, V. Valuev, M. Weber

University of California, Riverside, Riverside, USA

E. Bouvier, K. Burt, R. Clare, J. Ellison, J.W. Gary, S.M.A. Ghiasi Shirazi, G. Hanson, J. Heilman, P. Jandir, E. Kennedy, F. Lacroix, O.R. Long, M. Olmedo Negrete, M.I. Paneva, A. Shrinivas, W. Si, H. Wei, S. Wimpenny, B. R. Yates

University of California, San Diego, La Jolla, USA

J.G. Branson, G.B. Cerati, S. Cittolin, M. Derdzinski, R. Gerosa, A. Holzner, D. Klein, V. Krutelyov, J. Letts, I. Macneill, D. Olivito, S. Padhi, M. Pieri, M. Sani, V. Sharma, S. Simon, M. Tadel, A. Vartak, S. Wasserbaech⁶⁵, C. Welke, J. Wood, F. Würthwein, A. Yagil, G. Zevi Della Porta

University of California, Santa Barbara - Department of Physics, Santa Barbara, USA

N. Amin, R. Bhandari, J. Bradmiller-Feld, C. Campagnari, A. Dishaw, V. Dutta, M. Franco Sevilla, C. George, F. Golf, L. Gouskos, J. Gran, R. Heller, J. Incandela, S.D. Mullin, A. Ovcharova, H. Qu, J. Richman, D. Stuart, I. Suarez, J. Yoo

California Institute of Technology, Pasadena, USA

D. Anderson, J. Bendavid, A. Bornheim, J. Bunn, J. Duarte, J.M. Lawhorn, A. Mott, H.B. Newman, C. Pena, M. Spiropulu, J.R. Vlimant, S. Xie, R.Y. Zhu

Carnegie Mellon University, Pittsburgh, USA

M.B. Andrews, T. Ferguson, M. Paulini, J. Russ, M. Sun, H. Vogel, I. Vorobiev, M. Weinberg

University of Colorado Boulder, Boulder, USA

J.P. Cumalat, W.T. Ford, F. Jensen, A. Johnson, M. Krohn, S. Leontsinis, T. Mulholland, K. Stenson, S.R. Wagner

Cornell University, Ithaca, USA

J. Alexander, J. Chaves, J. Chu, S. Dittmer, K. Mcdermott, N. Mirman, J.R. Patterson, A. Rinkevicius, A. Ryd, L. Skinnari, L. Soffi, S.M. Tan, Z. Tao, J. Thom, J. Tucker, P. Wittich, M. Zientek

Fairfield University, Fairfield, USA

D. Winn

Fermi National Accelerator Laboratory, Batavia, USA

S. Abdullin, M. Albrow, G. Apollinari, A. Apresyan, S. Banerjee, L.A.T. Bauerdick, A. Beretvas, J. Berryhill, P.C. Bhat, G. Bolla, K. Burkett, J.N. Butler, H.W.K. Cheung, F. Chlebana, S. Cihangir[†], M. Cremonesi, V.D. Elvira, I. Fisk, J. Freeman, E. Gottschalk, L. Gray, D. Green, S. Grünendahl, O. Gutsche, D. Hare, R.M. Harris, S. Hasegawa, J. Hirschauer, Z. Hu, B. Jayatilaka, S. Jindariani, M. Johnson, U. Joshi, B. Klima, B. Kreis, S. Lammel, J. Linacre, D. Lincoln, R. Lipton, M. Liu, T. Liu, R. Lopes De Sá, J. Lykken, K. Maeshima, N. Magini, J.M. Marraffino, S. Maruyama, D. Mason, P. McBride, P. Merkel, S. Mrenna, S. Nahn, V. O'Dell, K. Pedro, O. Prokofyev, G. Rakness, L. Ristori, E. Sexton-Kennedy, A. Soha, W.J. Spalding, L. Spiegel, S. Stoynev, J. Strait, N. Strobbe, L. Taylor, S. Tkaczyk, N.V. Tran, L. Uplegger, E.W. Vaandering, C. Vernieri, M. Verzocchi, R. Vidal, M. Wang, H.A. Weber, A. Whitbeck, Y. Wu

University of Florida, Gainesville, USA

D. Acosta, P. Avery, P. Bortignon, D. Bourilkov, A. Brinkerhoff, A. Carnes, M. Carver, D. Curry, S. Das, R.D. Field, I.K. Furic, J. Konigsberg, A. Korytov, J.F. Low, P. Ma, K. Matchev, H. Mei, G. Mitselmakher, D. Rank, L. Shchutska, D. Sperka, L. Thomas, J. Wang, S. Wang, J. Yelton

Florida International University, Miami, USA

S. Linn, P. Markowitz, G. Martinez, J.L. Rodriguez

Florida State University, Tallahassee, USA

A. Ackert, T. Adams, A. Askew, S. Bein, S. Hagopian, V. Hagopian, K.F. Johnson, T. Kolberg, T. Perry, H. Prosper, A. Santra, R. Yohay

Florida Institute of Technology, Melbourne, USA

M.M. Baarmand, V. Bhopatkar, S. Colafranceschi, M. Hohlmann, D. Noonan, T. Roy, F. Yumiceva

University of Illinois at Chicago (UIC), Chicago, USA

M.R. Adams, L. Apanasevich, D. Berry, R.R. Betts, R. Cavanaugh, X. Chen, O. Evdokimov, C.E. Gerber, D.A. Hangal, D.J. Hofman, K. Jung, J. Kamin, I.D. Sandoval Gonzalez, H. Trauger, N. Varelas, H. Wang, Z. Wu, J. Zhang

The University of Iowa, Iowa City, USA

B. Bilki⁶⁶, W. Clarida, K. Dilsiz, S. Durgut, R.P. Gandrajula, M. Haytmyradov, V. Khristenko, J.-P. Merlo, H. Mermerkaya⁶⁷, A. Mestvirishvili, A. Moeller, J. Nachtman, H. Ogul, Y. Onel, F. Ozok⁶⁸, A. Penzo, C. Snyder, E. Tiras, J. Wetzel, K. Yi

Johns Hopkins University, Baltimore, USA

B. Blumenfeld, A. Cocoros, N. Eminizer, D. Fehling, L. Feng, A.V. Gritsan, P. Maksimovic, J. Roskes, U. Sarica, M. Swartz, M. Xiao, C. You

The University of Kansas, Lawrence, USA

A. Al-bataineh, P. Baringer, A. Bean, S. Boren, J. Bowen, J. Castle, L. Forthomme, S. Khalil, A. Kropivnitskaya, D. Majumder, W. Mcbrayer, M. Murray, S. Sanders, R. Stringer, J.D. Tapia Takaki, Q. Wang

Kansas State University, Manhattan, USA

A. Ivanov, K. Kaadze, Y. Maravin, A. Mohammadi, L.K. Saini, N. Skhirtladze, S. Toda

Lawrence Livermore National Laboratory, Livermore, USA

F. Rebassoo, D. Wright

University of Maryland, College Park, USA

C. Anelli, A. Baden, O. Baron, A. Belloni, B. Calvert, S.C. Eno, C. Ferraioli, J.A. Gomez, N.J. Hadley, S. Jabeen, G.Y. Jeng, R.G. Kellogg, J. Kunkle, A.C. Mignerey, F. Ricci-Tam, Y.H. Shin, A. Skuja, M.B. Tonjes, S.C. Tonwar

Massachusetts Institute of Technology, Cambridge, USA

D. Abercrombie, B. Allen, A. Apyan, V. Azzolini, R. Barbieri, A. Baty, R. Bi, K. Bierwagen, S. Brandt, W. Busza, I.A. Cali, M. D'Alfonso, Z. Demiragli, G. Gomez Ceballos, M. Goncharov, D. Hsu, Y. Iiyama, G.M. Innocenti, M. Klute, D. Kovalskyi, K. Krajczar, Y.S. Lai, Y.-J. Lee, A. Levin, P.D. Luckey, B. Maier, A.C. Marini, C. McGinn, C. Mironov, S. Narayanan, X. Niu, C. Paus, C. Roland, G. Roland, J. Salfeld-Nebgen, G.S.F. Stephans, K. Tatar, D. Velicanu, J. Wang, T.W. Wang, B. Wyslouch

University of Minnesota, Minneapolis, USA

A.C. Benvenuti, R.M. Chatterjee, A. Evans, P. Hansen, S. Kalafut, S.C. Kao, Y. Kubota, Z. Lesko, J. Mans, S. Nourbakhsh, N. Ruckstuhl, R. Rusack, N. Tambe, J. Turkewitz

University of Mississippi, Oxford, USA

J.G. Acosta, S. Oliveros

University of Nebraska-Lincoln, Lincoln, USA

E. Avdeeva, K. Bloom, D.R. Claes, C. Fangmeier, R. Gonzalez Suarez, R. Kamalieddin, I. Kravchenko, A. Malta Rodrigues, J. Monroy, J.E. Siado, G.R. Snow, B. Stieger

State University of New York at Buffalo, Buffalo, USA

M. Alyari, J. Dolen, A. Godshalk, C. Harrington, I. Iashvili, J. Kaisen, D. Nguyen, A. Parker, S. Rappoccio, B. Roozbahani

Northeastern University, Boston, USA

G. Alverson, E. Barberis, A. Hortiangtham, A. Massironi, D.M. Morse, D. Nash, T. Orimoto, R. Teixeira De Lima, D. Trocino, R.-J. Wang, D. Wood

Northwestern University, Evanston, USA

S. Bhattacharya, O. Charaf, K.A. Hahn, N. Mucia, N. Odell, B. Pollack, M.H. Schmitt, K. Sung, M. Trovato, M. Velasco

University of Notre Dame, Notre Dame, USA

N. Dev, M. Hildreth, K. Hurtado Anampa, C. Jessop, D.J. Karmgard, N. Kellams, K. Lannon, N. Marinelli, F. Meng, C. Mueller, Y. Musienko³⁴, M. Planer, A. Reinsvold, R. Ruchti, N. Rupperecht, G. Smith, S. Taroni, M. Wayne, M. Wolf, A. Woodard

The Ohio State University, Columbus, USA

J. Alimena, L. Antonelli, B. Bylsma, L.S. Durkin, S. Flowers, B. Francis, A. Hart, C. Hill, W. Ji, B. Liu, W. Luo, D. Puigh, B.L. Winer, H.W. Wulsin

Princeton University, Princeton, USA

S. Cooperstein, O. Driga, P. Elmer, J. Hardenbrook, P. Hebda, D. Lange, J. Luo, D. Marlow, T. Medvedeva, K. Mei, I. Ojalvo, J. Olsen, C. Palmer, P. Piroué, D. Stickland, A. Svyatkovskiy, C. Tully

University of Puerto Rico, Mayaguez, USA

S. Malik

Purdue University, West Lafayette, USA

A. Barker, V.E. Barnes, S. Folgueras, L. Gutay, M.K. Jha, M. Jones, A.W. Jung, A. Khatiwada, D.H. Miller, N. Neumeister, J.F. Schulte, X. Shi, J. Sun, F. Wang, W. Xie

Purdue University Northwest, Hammond, USA

N. Parashar, J. Stupak

Rice University, Houston, USA

A. Adair, B. Akgun, Z. Chen, K.M. Ecklund, F.J.M. Geurts, M. Guilbaud, W. Li, B. Michlin, M. Northup, B.P. Padley, J. Roberts, J. Rorie, Z. Tu, J. Zabel

University of Rochester, Rochester, USA

B. Betchart, A. Bodek, P. de Barbaro, R. Demina, Y.t. Duh, T. Ferbel, M. Galanti, A. Garcia-Bellido, J. Han, O. Hindrichs, A. Khukhunaishvili, K.H. Lo, P. Tan, M. Verzetti

Rutgers, The State University of New Jersey, Piscataway, USA

A. Agapitos, J.P. Chou, Y. Gershtein, T.A. Gómez Espinosa, E. Halkiadakis, M. Heindl, E. Hughes, S. Kaplan, R. Kunnawalkam Elayavalli, S. Kyriacou, A. Lath, R. Montalvo, K. Nash, M. Osherson, H. Saka, S. Salur, S. Schnetzer, D. Sheffield, S. Somalwar, R. Stone, S. Thomas, P. Thomassen, M. Walker

University of Tennessee, Knoxville, USA

A.G. Delannoy, M. Foerster, J. Heideman, G. Riley, K. Rose, S. Spanier, K. Thapa

Texas A&M University, College Station, USA

O. Bouhali⁶⁹, A. Celik, M. Dalchenko, M. De Mattia, A. Delgado, S. Dildick, R. Eusebi, J. Gilmore, T. Huang, E. Juska, T. Kamon⁷⁰, R. Mueller, Y. Pakhotin, R. Patel, A. Perloff, L. Perniè, D. Rathjens, A. Safonov, A. Tatarinov, K.A. Ulmer

Texas Tech University, Lubbock, USA

N. Akchurin, J. Damgov, F. De Guio, C. Dragoiu, P.R. Duderø, J. Faulkner, E. Gurpinar, S. Kunori, K. Lamichhane, S.W. Lee, T. Libeiro, T. Peltola, S. Undleeb, I. Volobouev, Z. Wang

Vanderbilt University, Nashville, USA

S. Greene, A. Gurrola, R. Janjam, W. Johns, C. Maguire, A. Melo, H. Ni, P. Sheldon, S. Tuo, J. Velkovska, Q. Xu

University of Virginia, Charlottesville, USA

M.W. Arenton, P. Barria, B. Cox, R. Hirosky, A. Ledovskoy, H. Li, C. Neu, T. Sinthuprasith, X. Sun, Y. Wang, E. Wolfe, F. Xia

Wayne State University, Detroit, USA

C. Clarke, R. Harr, P.E. Karchin, J. Sturdy, S. Zaleski

University of Wisconsin - Madison, Madison, WI, USA

D.A. Belknap, J. Buchanan, C. Caillol, S. Dasu, L. Dodd, S. Duric, B. Gomber, M. Grothe, M. Herndon, A. Hervé, U. Hussain, P. Klabbers, A. Lanaro, A. Levine, K. Long, R. Loveless, G.A. Pierro, G. Polese, T. Ruggles, A. Savin, N. Smith, W.H. Smith, D. Taylor, N. Woods

†: Deceased

- 1: Also at Vienna University of Technology, Vienna, Austria
- 2: Also at State Key Laboratory of Nuclear Physics and Technology, Peking University, Beijing, China
- 3: Also at Universidade Estadual de Campinas, Campinas, Brazil
- 4: Also at Universidade Federal de Pelotas, Pelotas, Brazil
- 5: Also at Université Libre de Bruxelles, Bruxelles, Belgium
- 6: Also at Universidad de Antioquia, Medellin, Colombia
- 7: Also at Joint Institute for Nuclear Research, Dubna, Russia
- 8: Also at Suez University, Suez, Egypt
- 9: Now at British University in Egypt, Cairo, Egypt
- 10: Also at Ain Shams University, Cairo, Egypt
- 11: Now at Helwan University, Cairo, Egypt
- 12: Also at Université de Haute Alsace, Mulhouse, France
- 13: Also at Skobeltsyn Institute of Nuclear Physics, Lomonosov Moscow State University, Moscow, Russia
- 14: Also at CERN, European Organization for Nuclear Research, Geneva, Switzerland
- 15: Also at RWTH Aachen University, III. Physikalisches Institut A, Aachen, Germany
- 16: Also at University of Hamburg, Hamburg, Germany
- 17: Also at Brandenburg University of Technology, Cottbus, Germany
- 18: Also at Institute of Nuclear Research ATOMKI, Debrecen, Hungary
- 19: Also at MTA-ELTE Lendület CMS Particle and Nuclear Physics Group, Eötvös Loránd University, Budapest, Hungary
- 20: Also at Institute of Physics, University of Debrecen, Debrecen, Hungary
- 21: Also at Indian Institute of Technology Bhubaneswar, Bhubaneswar, India
- 22: Also at University of Visva-Bharati, Santiniketan, India
- 23: Also at Institute of Physics, Bhubaneswar, India
- 24: Also at University of Ruhuna, Matara, Sri Lanka
- 25: Also at Isfahan University of Technology, Isfahan, Iran
- 26: Also at Yazd University, Yazd, Iran
- 27: Also at Plasma Physics Research Center, Science and Research Branch, Islamic Azad University, Tehran, Iran
- 28: Also at Università degli Studi di Siena, Siena, Italy
- 29: Also at Purdue University, West Lafayette, USA
- 30: Also at International Islamic University of Malaysia, Kuala Lumpur, Malaysia
- 31: Also at Malaysian Nuclear Agency, MOSTI, Kajang, Malaysia
- 32: Also at Consejo Nacional de Ciencia y Tecnología, Mexico city, Mexico
- 33: Also at Warsaw University of Technology, Institute of Electronic Systems, Warsaw, Poland
- 34: Also at Institute for Nuclear Research, Moscow, Russia
- 35: Now at National Research Nuclear University 'Moscow Engineering Physics Institute' (MEPhI), Moscow, Russia
- 36: Also at St. Petersburg State Polytechnical University, St. Petersburg, Russia
- 37: Also at University of Florida, Gainesville, USA
- 38: Also at P.N. Lebedev Physical Institute, Moscow, Russia
- 39: Also at California Institute of Technology, Pasadena, USA
- 40: Also at Budker Institute of Nuclear Physics, Novosibirsk, Russia
- 41: Also at Faculty of Physics, University of Belgrade, Belgrade, Serbia
- 42: Also at INFN Sezione di Roma; Sapienza Università di Roma, Roma, Italy
- 43: Also at University of Belgrade, Faculty of Physics and Vinca Institute of Nuclear Sciences,

Belgrade, Serbia

44: Also at Scuola Normale e Sezione dell'INFN, Pisa, Italy

45: Also at National and Kapodistrian University of Athens, Athens, Greece

46: Also at Riga Technical University, Riga, Latvia

47: Also at Institute for Theoretical and Experimental Physics, Moscow, Russia

48: Also at Albert Einstein Center for Fundamental Physics, Bern, Switzerland

49: Also at Gaziosmanpasa University, Tokat, Turkey

50: Also at Adiyaman University, Adiyaman, Turkey

51: Also at Istanbul Aydin University, Istanbul, Turkey

52: Also at Mersin University, Mersin, Turkey

53: Also at Cag University, Mersin, Turkey

54: Also at Piri Reis University, Istanbul, Turkey

55: Also at Ozyegin University, Istanbul, Turkey

56: Also at Izmir Institute of Technology, Izmir, Turkey

57: Also at Marmara University, Istanbul, Turkey

58: Also at Kafkas University, Kars, Turkey

59: Also at Istanbul Bilgi University, Istanbul, Turkey

60: Also at Yildiz Technical University, Istanbul, Turkey

61: Also at Hacettepe University, Ankara, Turkey

62: Also at Rutherford Appleton Laboratory, Didcot, United Kingdom

63: Also at School of Physics and Astronomy, University of Southampton, Southampton, United Kingdom

64: Also at Instituto de Astrofísica de Canarias, La Laguna, Spain

65: Also at Utah Valley University, Orem, USA

66: Also at BEYKENT UNIVERSITY, Istanbul, Turkey

67: Also at Erzincan University, Erzincan, Turkey

68: Also at Mimar Sinan University, Istanbul, Istanbul, Turkey

69: Also at Texas A&M University at Qatar, Doha, Qatar

70: Also at Kyungpook National University, Daegu, Korea